Cell

Structure, receptor recognition, and antigenicity of the human coronavirus CCoV-HuPn-2018 spike glycoprotein

Graphical abstract
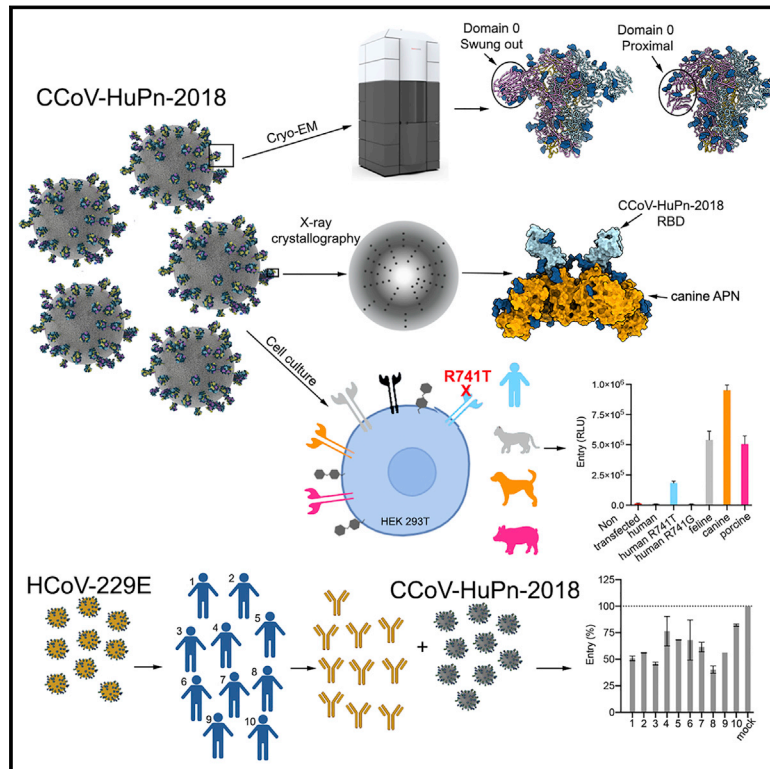
Authors
M. Alejandra Tortorici, Alexandra C. Walls, Anshu Joshi, ..., Davide Corti, Jesse D. Bloom, David Veesler

Correspondence
dveesler@uw.edu

In brief
Cryo-EM structures of the coronavirus CCoV-HuPn-2018 S reveal two conformations of domain 0, which recognize sialosides. Canine, feline, and porcine APNs and human N739 glycan knockin APN are entry receptors, suggesting that SNPs might account for CCoV-HuPn-2018 detection in patients. Human antibodies elicited by coronavirus 229E infection inhibit CCoV-HuPn-2018, highlighting α-coronavirus cross-neutralizing activity.

Highlights

- Cryo-EM structures of CCoV-HuPn-2018 S reveal two conformational states of domain 0

- Canine, feline, porcine APN orthologs mediate S-mediated entry

- Engineering N739 glycan in human APN enables CCoV-HuPn-2018 entry

- Plasma from HCoV-229E-infected subjects inhibit CCoV-HuPn-2018 S-mediated entry

CellPress

Cell

Article

Structure, receptor recognition, and antigenicity of the human coronavirus CCoV-HuPn-2018 spike glycoprotein

M. Alejandra Tortorici,[1] Alexandra C. Walls,[1,2] Anshu Joshi,[1] Young-Jun Park,[1] Rachel T. Eguia,[3] Marcos C. Miranda,[1,4] Elizabeth Kepl,[1,4] Annie Dosey,[1,4] Terry Stevens-Ayers,[5] Michael J. Boeckh,[5] Amalio Telenti,[6] Antonio Lanzavecchia,[7,8] Neil P. King,[1,4] Davide Corti,[8] Jesse D. Bloom,[3] and David Veesler[1,2,9,*]

[1]Department of Biochemistry, University of Washington, Seattle, WA 98195, USA
[2]Howard Hughes Medical Institute, University of Washington, Seattle, WA 98195, USA
[3]Basic Sciences Division, Fred Hutchinson Cancer Research Center, Seattle, WA 98109, USA
[4]Institute for Protein Design, University of Washington, Seattle, WA 98195, USA
[5]Vaccine and Infectious Disease Division, Fred Hutchinson Cancer Research Center, Seattle, WA 98109, USA
[6]Vir Biotechnology, San Francisco, CA 94158, USA
[7]Istituto Nazionale Genetica Molecolare, 20122 Milano, Italy
[8]Humabs Biomed SA–a subsidiary of Vir Biotechnology, 6500 Bellinzona, Switzerland
[9]Lead contact
*Correspondence: dveesler@uw.edu
https://doi.org/10.1016/j.cell.2022.05.019

SUMMARY

The isolation of CCoV-HuPn-2018 from a child respiratory swab indicates that more coronaviruses are spilling over to humans than previously appreciated. We determined the structures of the CCoV-HuPn-2018 spike glycoprotein trimer in two distinct conformational states and showed that its domain 0 recognizes sialosides. We identified that the CCoV-HuPn-2018 spike binds canine, feline, and porcine aminopeptidase N (APN) orthologs, which serve as entry receptors, and determined the structure of the receptor-binding B domain in complex with canine APN. The introduction of an oligosaccharide at position N739 of human APN renders cells susceptible to CCoV-HuPn-2018 spike-mediated entry, suggesting that single-nucleotide polymorphisms might account for viral detection in some individuals. Human polyclonal plasma antibodies elicited by HCoV-229E infection and a porcine coronavirus monoclonal antibody inhibit CCoV-HuPn-2018 spike-mediated entry, underscoring the cross-neutralizing activity among α-coronaviruses. These data pave the way for vaccine and therapeutic development targeting this zoonotic pathogen representing the eighth human-infecting coronavirus.

INTRODUCTION

Four coronaviruses are endemic in humans and typically responsible for common colds: the β-coronaviruses HCoV-OC43 and HKU1 and the α-coronaviruses HCoV-NL63 and HCoV-229E. Moreover, three highly pathogenic β-coronaviruses have jumped from their animal hosts to humans in the last two decades: SARS-CoV, MERS-CoV, and SARS-CoV-2. Recurrent coronavirus zoonoses along with detection of numerous coronaviruses in wildlife suggest that cross-species transmission events will continue to occur (Anthony et al., 2017; Delaune et al., 2021; Menachery et al., 2015, 2016, 2020).

The coronavirus spike (S) glycoprotein folds as a homotrimer promoting viral entry into host cells (Tortorici and Veesler, 2019; Walls et al., 2016a, 2020a). S comprises an S_1 subunit, which recognizes host cell receptors, and an S_2 subunit, that mediates fusion of the viral and cellular membranes (Walls et al.,

2017). Therefore, S plays a key role in modulating host and tissue tropism as well as zoonotic transmission. Since the coronavirus S glycoprotein is the target of neutralizing antibodies, it is the main focus of therapeutics and vaccine development, including monoclonal antibody therapies. (Arunachalam et al., 2021; Baum et al., 2020; Corbett et al., 2020; Corti et al., 2021; Hansen et al., 2020; McCallum et al., 2021a; Park et al., 2022; Piccoli et al., 2020; Pinto et al., 2020; Polack et al., 2020; Walls et al., 2019, 2020b, 2021).

Viruses genetically related to canine and feline coronaviruses have been previously identified in respiratory swabs obtained from patients with pneumonia or acute respiratory symptoms in Malaysia and the US (Silva and Mullis, 2014; Xiu et al., 2020). In Malaysia, eight out of 301 (2.5%) patients hospitalized with pneumonia between 2017 and 2018 in Sarawak were positive by pan-species coronavirus semi-nested RT-PCR assay, and one specimen was identified as a novel canine-feline
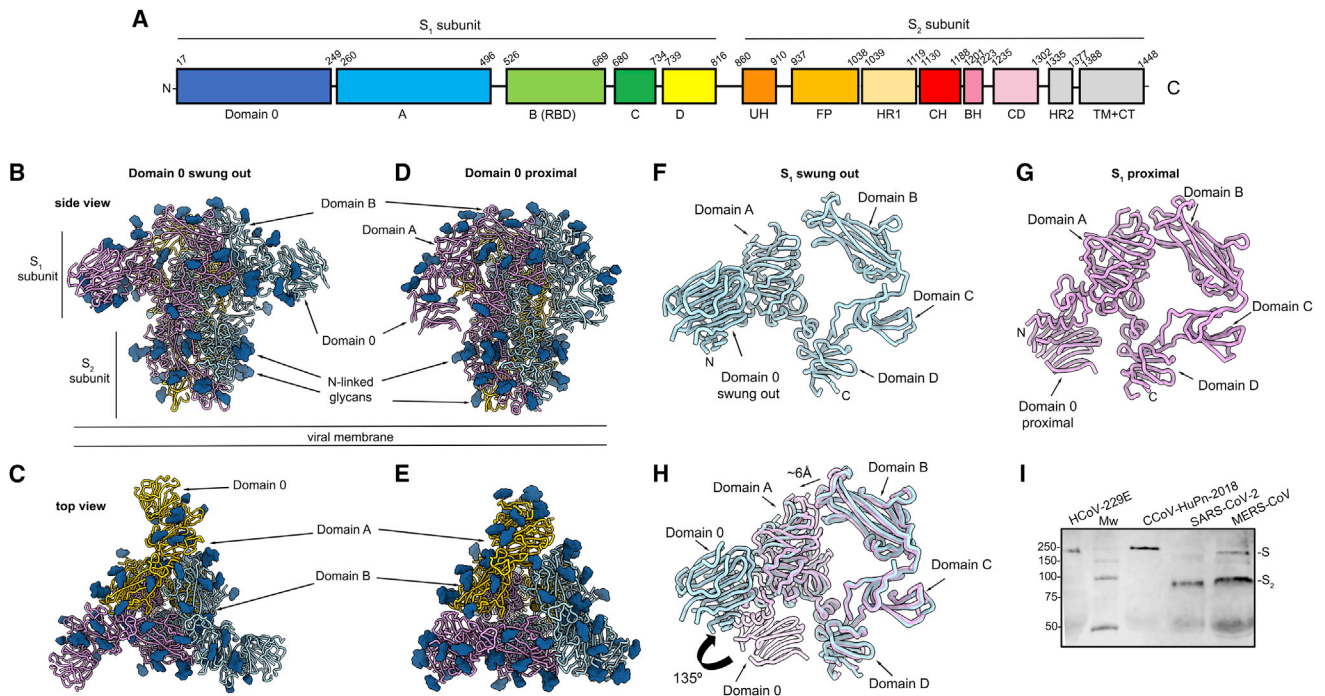
Figure 1. Architecture of the CCoV-HuPn-2018 infection machinery

(A) Schematic diagram of the S glycoprotein organization. UH, upstream helix; FP, fusion peptide; HR1, heptad-repeat 1; CH, central helix; BH, β-hairpin; CD, connector domain; HR2, heptad-repeat 2; TM, transmembrane domain; CT, cytoplasmic tail. Gray boxes denote regions unresolved in the reconstruction (HR2) and regions that were not part of the construct (TM and CT), respectively.

(B and C) Cryo-EM structure of the CCoV-HuPn-2018 S ectodomain trimer (with each domain 0 swung out) viewed along two orthogonal orientations.

(D and E) Cryo-EM structure of the CCoV-HuPn-2018 S ectodomain trimer (with each domain 0 pointing "proximal" toward the viral membrane) viewed along two orthogonal orientations.

(F and G) Ribbon diagram of the CCoV-HuPn-2018 S_1 subunit with domain 0 in the swung out (F) and proximal (G) conformations.

(H) Superimposition of the S_1 subunit from the structures with domain 0 in the swung out (light blue) and proximal (pink) conformations showing the A domain moving away from the B domain of the same protomer and rotation of domain 0.

Renderings in (B–H) use composite models obtained from the global and local refinements for each conformation.

(I) Western blot of VSV pseudotyped particles harboring HCoV-229E S, CCoV-HuPn-2018 S, SARS-CoV-2 S, and MERS-CoV S. MW, molecular weight ladder. Full-length S and S_2 subunit bands are indicated on the right-hand side of the blot.

See also Figures S1 and S2 and Tables S1 and S2.

recombinant alphacoronavirus (genotype II) that was named CCoV-HuPn-2018 (Vlasova et al., 2021). The coronavirus isolate was shown to be cytopathic using canine A72 cells (Vlasova et al., 2021). A closely related virus (HuCCoV_Z19Haiti) harboring a S glycoprotein differing by only two amino acids was subsequently identified in Florida from urine samples of travelers coming back from Haiti (Lednicky et al., 2021a). These studies suggested that zoonotic transmission occurred and that these viruses, which were not previously known to infect humans, might be associated with clinical symptoms. Furthermore, these findings point to the circulation of several more coronaviruses in humans than previously appreciated and underscore the zoonotic threats posed by members of multiple distinct coronavirus genera.

RESULTS

Architecture of the CCoV-HuPn-2018 S trimer

To visualize the infection machinery of the newly emerged CCoV-HuPn-2018, we characterized its S glycoprotein ectodo-

main trimer using cryoelectron microscopy (cryo-EM). The CCoV-HuPn-2018 S trimer is ∼150Å high with a triangular cross-section and comprises an N-terminal S_1 subunit divided into domains designated 0 and A–D as well as a C-terminal S_2 subunit, which contains the fusion machinery (Tortorici and Veesler, 2019; Figure 1A). 3D classification of the data revealed the presence of two distinct S conformations with domain 0 swung out (at the periphery of the trimer) or proximal, i.e., oriented toward the viral membrane (apposed directly underneath domain A) for which we determined structures at 2.8- and 3.1-Å resolution, respectively (Figures 1B–1G and S1; Table S1). The latter domain 0 conformational state ("proximal") is similar to the one described for the S of HCoV-NL63 (Walls et al., 2016b) and porcine epidemic diarrhea virus (PEDV) (Kirchdoerfer et al., 2021), whereas the former conformation ("swung out") is more reminiscent of another state detected for PEDV S (Wrapp and McLellan, 2019) and feline infectious peritonitis virus (FIPV) (Figure S2). We used local refinement to overcome the conformational variability of domain 0 and obtained reconstructions at 3.1- and 3.8-Å resolution for the swung-out and proximal

conformational states, respectively, which are related by a rotation of 135° (Figures 1H and S1; Table S1).

The CCoV-HuPn-2018 S trimer is densely decorated with oligosaccharides distributed in both the S_1 and S_2 subunits. In total, 22 glycans out of 32 putative N-linked glycosylation sequons in CCoV-HuPn-2018 S ectodomain are resolved to different extents in at least one of the two cryo-EM maps (Figures 1B–1E; Table S2). The S_1 subunit structure is most similar to HCoV-NL63 and HCoV-229E S whereas the S_2 subunit architecture is most closely related to PEDV and FIPV S, supporting the possibility that the CCoV-HuPn-2018 S gene arose from a recombination event (Vlasova et al., 2021). Although the B domains remain in a closed state, i.e., sitting atop the fusion machinery, in both CCoV-HuPn-2018 S conformations, the two structures differ in the tertiary and quaternary organization of the S_1 subunit crown. Specifically, domain A moves radially outward upon transition from a proximal to a swung-out domain 0 conformation, positioning it >6 Å further away from the B domain belonging to the same protomer (Figures 1F–1H). As a result, domain A moves closer to and forms tight interactions with the C domain of a neighboring protomer in the swung-out domain 0 state. Overall, interactions among C domains contribute to a marked enhancement of the total surface area buried between S_1 protomers (stabilizing the S_1 trimer), whereas the B domains reduce tertiary and quaternary contacts with their surroundings upon transition to the swung-out conformation, likely enabling subsequent opening and receptor engagement.

The CCoV-HuPn-2018 S lacks a polybasic furin cleavage site at the S_1/S_2 junction, similar to type-II feline and canine coronaviruses (Licitra et al., 2013; Millet and Whittaker, 2015). Accordingly, we did not detect proteolytic processing of CCoV-HuPn-2018 S in vesicular stomatitis virus (VSV) particles pseudotypes produced in HEK293T cells, similar to HCoV-229E S VSV (Figure 1G). In contrast, SARS-CoV-2 S or MERS-CoV S VSV pseudotypes were cleaved at S_1/S_2 by furin-like proteases (Figure 1G; Millet and Whittaker, 2014, 2015; Walls et al., 2020a). The CCoV-HuPn-2018 S_2' site contains a polybasic motif $K_{953}RKYR_{957}$, which is identical to the one found in transmissible gastroenteritis virus (TGEV) S and some type II feline and canine coronavirus S sequences (Millet and Whittaker, 2015) and might modulate cleavage and infectivity.

Organization of the CCoV-HuPn-2018 S_1 subunit

Coronaviruses can use multiple domains within the S_1 subunit for receptor attachment and some coronavirus spike glycoproteins engage more than one receptor type to enter host cells (Hulswit et al., 2019; Lempp et al., 2021; Li et al., 2017; Park et al., 2019; Peng et al., 2011; Tortorici et al., 2019). CCoV-HuPn-2018 domain A folds as a galectin-like β-sandwich and most closely resembles the equivalent domains of α-coronavirus S glycoproteins including HCoV-NL63 (Walls et al., 2016b), HCoV-229E (Li et al., 2019), PEDV (Kirchdoerfer et al., 2021; Wrapp and McLellan, 2019), and FIPV (Hsu et al., 2020) with which it shares ~40% sequence identity. Superimposition of the CoV-HuPn-2018 S 0 and A domains underscores their conserved architecture and topology (RMSD 4.2 Å over 139 aligned Cα positions) although they share only 12.5% sequence identity (Figures 2A–2G). These

findings suggest that both domains derived from an ancestral gene duplication event, as previously described for HCoV-NL63 (Walls et al., 2016b), and accumulated extensive mutations leading to their very low sequence relatedness.

The CCoV-HuPn-2018 domain B structure is strikingly similar to the porcine respiratory coronavirus (PRCV) and TGEV domain B structures (Reguera et al., 2012) with which it shares ~90% sequence identity, including key aminopeptidase N (APN) interacting residues (PRCV Y320/W363, based on sequence code P27655.1, corresponding to CCoV-HuPn-2018 Y543/W586) (Figures S3A–S3C). Although the β-sandwich fold is also shared with HCoV-NL63, HCoV-229E, and porcine delta-coronavirus, their receptor-binding loops adopt distinct conformations compared with CCoV-HuPn-2018, PRCV, and TGEV (Reguera et al., 2012; Shang et al., 2018; Wong et al., 2017; Wu et al., 2009; Xiong et al., 2018; Figures S3D–S3G).

CCoV-HuPn-2018 S domain 0 hemagglutinates human erythrocytes in a sialic-acid-dependent manner

Although some β-coronaviruses, such as MERS-CoV, use both proteinaceous and sialoglycan receptors to enter target cells (Li et al., 2017; Lu et al., 2013; Park et al., 2019), other β-coronaviruses, including HCoV-OC43, HCoV-HKU1, and bovine CoV (BCoV), appear to rely only on sialoglycan receptors for cell entry (Li et al., 2017; Tortorici et al., 2019; Vlasak et al., 1988). To investigate whether CCoV-HuPn-2018 S could recognize sialoglycans, we evaluated the ability of individual S domains to hemagglutinate erythrocytes. Since interactions with carbohydrate receptors are typically of low affinity, we multivalently displayed CCoV-HuPn-2018 S domain 0, A, or B at the surface of the two-component protein nanoparticle (NP) I53-50 (Bale et al., 2016; Figure S4). HCoV-HKU1 S I53-50 NP and influenza virus hemagglutinin (HA)-ferritin NP (H1N1 A/New Caledonia/99) were used as positive controls (Figure 3A). NPs displaying CCoV-HuPn-2018 S domain 0, but not the A or B domains, hemagglutinated turkey, canine, and human erythrocytes in a concentration-dependent manner (Figures 3A and 3B). No hemagglutination was observed, however, when human erythrocytes were desialylated by pretreatment with neuraminidase, similar to observations made for MERS-CoV domain A (Li et al., 2017; Figure 3C). These results indicate that the CCoV-HuPn-2018 S domain 0 is responsible for the observed hemagglutination of erythrocytes, which is sialic-acid-dependent and likely associated with the attachment process during cell entry.

Aminopeptidase N is a receptor for CCoV-HuPn-2018

Based on the structural similarity between the B domain of CCoV-HuPn-2018 and other α-coronaviruses such as PRCV and TGEV (Figures S3A–S3C), we evaluated the ability of the CCoV-HuPn-2018 B domain to interact with several APN orthologs, which is the proteinaceous receptor for both PRCV and TGEV (Delmas et al., 1992). Dimeric feline, canine, and porcine APNs, but not human APN, recognized the biotinylated CCoV-HuPn-2018 B domain immobilized at the surface of biolayer interferometry biosensors (Figures 4A–4D). The CCoV-HuPn-2018 B domain bound with higher avidity to canine APN ($K_{D,app}$ = 1.0 nM) compared with feline APN ($K_{D,app}$ = 27 nM) and porcine APN ($K_{D,app}$ = 41 nM), as was the case for the TGEV B domain (Figures 4A–4D and 4F–4I;
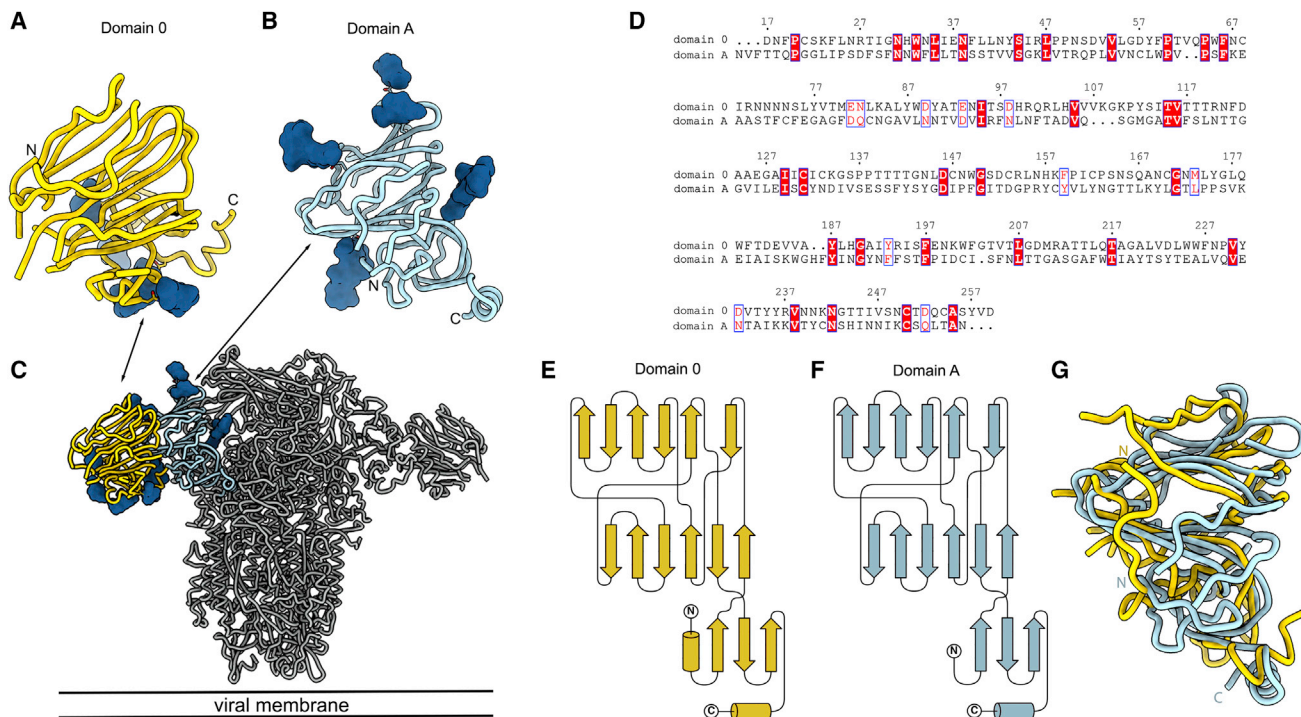
Figure 2. Structural conservation of CCoV-HuPn-2018 S domain 0 and domain A

(A–C) Ribbon diagrams of the CCoV-HuPn-2018 S domain 0 (A) and domain A (B) oriented as shown in the prefusion S conformation in (C). Rendering in (C) uses a composite model obtained from the global and local refinements.

(D) Sequence alignment of CCoV-HuPn-2018 S domain A and domain 0 highlighting the low sequence identity (12.5%) between them.

(E–G) Topology diagrams of domain 0 (E) and domain A (F) and structural overlay between the two domains (G) underscoring their similarity.

N-linked glycans are rendered as blue spheres in (A)–(C) but were removed from (G) for clarity.

See also Figures S1 and S2 and Tables S1 and S2.

Table S3). We also evaluated the ability of the CCoV-HuPn-2018 B domain to interact with several APN orthologs by pull-down assays and found that feline, canine, and porcine APNs, but not human APN, recognized biotinylated CCoV-HuPn-2018 and TGEV B domains coupled to streptavidin beads (Figures S5A, S5B, S5D, and S5E). Human APN, however, interacted with the HCoV-229E B domain as observed by pull-down and biolayer interferometry (Figures S5C–S5E, S5G, and S5H; Table 3). These data suggest that CCoV-HuPn-2018 can use several APN orthologs as receptors likely involving a binding mode comparable to PRCV/TGEV but distinct from HCoV-229E (Reguera et al., 2012; Wong et al., 2017).

We determined a crystal structure of the complex between the CCoV-HuPn-2018 B domain and canine APN at 3.2 Å resolution to visualize the molecular basis of recognition (Table S4; Figures 4K–4M). Canine APN forms a crystallographic dimer and binds to CCoV-HuPn-2018 B through interactions reminiscent of those observed for PRCV B in complex with porcine APN (Figure 4M; Reguera et al., 2012). The CCoV-HuPn-2018 domain B Y543 side chain, which protrudes from receptor-binding loop 1, packs against the core fucose linked to canine APN N747 (human APN position 739) (Figure 4M) and is hydrogen bonded to APN E742 (human APN position 734) and W748 side chains (human APN position 740) (Figure 4M). PRCV B

Y320 interacts with the equivalent porcine APN residues E731 and W737. The R540 side chain in receptor-binding loop 1 forms a salt bridge with the APN E786 side chain (human APN position 778) (Figure 4M), whereas PRCV B R317 is electrostatically interacting with residue Q775 in porcine APN. CCoV-HuPn-2018 domain B Q545 side chain is hydrogen bonded to the canine APN N747 side chain (human APN position 739), the first N-linked NAG and to the core fucose. PRCV B Q322 forms identical interactions with porcine APN N736 and the first NAG. In receptor-binding loop 2, W586 is packed against APN residues Y797 and P798 (Figure 4M), and its imino group is hydrogen bonded to the main-chain carbonyl of N794 (human APN position 786). PRCV B W363 forms equivalent contacts with porcine APN residues H786, P787, and N783, respectively.

We next assessed the ability of various APN orthologs to promote cell entry of VSV particles pseudotyped with CCoV-HuPn-2018 S, TGEV S, or HCoV-229E S. Transient transfection of feline, canine, or porcine, but not human, APN, rendered HEK293T cells susceptible to CCoV-HuPn-2018 S VSV pseudovirus entry (Figure 5A), in line with the binding data (Figures 4A–4C). Feline, canine, and porcine APNs also promoted TGEV S pseudotyped virus entry into HEK293T cells (Figure 5B), whereas HCoV-229E-S-mediated entry occurred with feline or human APN, but not with canine or porcine orthologs (Figure 5C),
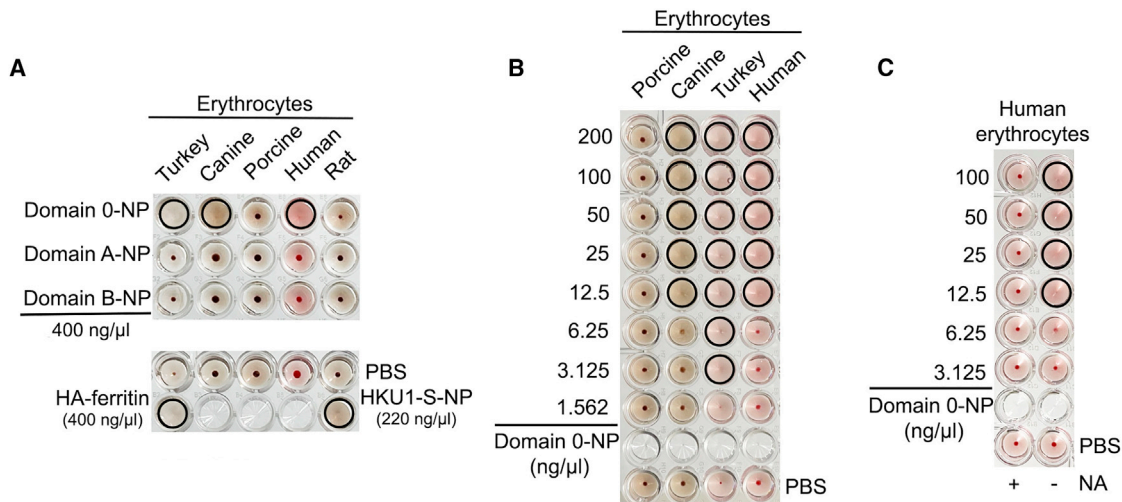
Figure 3. CCoV-HuPn-2018 S domain 0 recognizes sialic acid and hemagglutinates erythrocytes
(A) 50 μL of CCoV-HuPn-2018 domain 0, domain A, or domain B multivalently displayed at the surface of the I53-50 nanoparticle (NP) at 400 ng/μL were incubated with 50 μL of 0.5% (v/v) of turkey, canine, porcine, human, or rat erythrocytes for 30–45 min at room temperature before analysis of hemagglutination. As positive controls, 50 μL of hemagglutinin (HA)-ferritin (HA-ferritin, H1N1 A/New Caledonia/99) and HCoV-HKU1 S NP (HKU-1-S-NP) at 400 and 220 ng/μL were mixed with 50 μL of 0.5% (v/v) turkey or rat erythrocytes, respectively.
(B) Serial dilutions of CCoV-HuPn-2018 S domain 0-I53-50 NP (starting at 200 ng/μL) were incubated with the indicated erythrocytes to assess hemagglutination.
(C) Serial dilutions of CCoV-HuPn-2018 S domain 0 NP (starting at 100 ng/μL) were incubated with *Arthrobacter ureafaciens* neuraminidase (NA)-treated human erythrocytes to assess hemagglutination. Erythrocytes mixed with PBS were used as a negative control. Wells positive for hemagglutination are encircled. The experiments were carried out with two biological replicates (using distinct protein and erythrocyte batches) each with two technical replicates.
See also Figure S4.

concurring with previous data (Li et al., 2018). Co-transfection of TMPRSS2 with APN did not enhance CCoV-HuPn-2018 S or TGEV S pseudovirus entry (Figures 5D–5F), likely reflecting the ability to employ redundant proteolytic pathways for membrane fusion to occur at the plasma membrane or the endosomal membrane, similar to HCoV-229E (Bertram et al., 2013). We also observed CCoV-HuPn-2018 S VSV entry in canine A72 cells (Vlasova et al., 2021), Madin-Darby canine kidney (MDCK) cells, and Crandell-Rees feline kidney (CRFK) cells (Figure S6A), presumably due to endogenous APN expression. Among the cell lines evaluated, feline and one of the two canine cell lines permitted TGEV S VSV entry (Figure S6B), whereas only feline CRFK cells facilitated entry of 229E S pseudovirus (Figure S6C), concurring with the data obtained with transfected APN orthologs (Figures 5A–5C). Finally, we observed concentration-dependent inhibition of CCoV-HuPn-2018 S pseudotyped virus entry using purified dimeric feline, canine or porcine APN-Fc fusions (Figure 5G), establishing APN as a bona fide entry receptor for CCoV-HuPn-2018.

A key distinction between human APN and feline/canine/porcine APNs is the absence of an N-linked oligosaccharide at position N739 of the former ortholog due to a T to R residue substitution at position 741, which is position i + 2 of a glycosylation sequon (Figure 5H). Previous work showed that abrogation of this glycosylation site prevented binding of the TGEV RBD to cell-surface-expressed porcine APN and that mutations of residues i and i + 2 of this glycosylation sequon affected the receptor activity of feline APN for distinct α-coronaviruses (Reguera et al., 2012; Tusell et al., 2007). The structural conservation between

CCoV-HuPn-2018 and TGEV/PRCV B domains along with the interactions formed between the canine APN N747 glycan and the CCoV-HuPn-2018 B domain in our crystal structure (Figure 4M), suggest that the absence of this oligosaccharide in human APN might contribute to the lack of detectable binding and inability of CCoV-HuPn-2018 S to utilize human APN for cell entry. To evaluate this hypothesis, we generated a human APN N739 oligosaccharide knockin mutant (by introducing the R741T substitution) and assessed its ability to mediate pseudotyped virus entry. Human R741T APN rendered HEK293T cells permissive to both CCoV-HuPn-2018 and TGEV S-mediated entry (Figures 5A and 5B), and the human R741T APN-Fc inhibited CCoV-HuPn-2018 S pseudovirus entry in a concentration-dependent manner (Figure 5G). Conversely, the canine APN T749R oligosaccharide knockout mutant (human APN position 741) abolished binding to CCoV-HuPn-2018 B domain (Figure S5F) and entry of CCoV-HuPn-2018 S VSV into HEK293T cells transfected with this mutant APN (Figure 5I), confirming the key role of this post-translational modification for receptor recognition. As the human APN R741 side chain might sterically interfere with CCoV-HuPn-2018 and PRCV/TGEV B domain binding, we assessed whether human APN R741G, which is a rare single-nucleotide polymorphism found in humans and lacks the N739 glycan, could serve as entry receptor. Neither CCoV-HuPn-2018 S or TGEV S VSV pseudotypes could enter HEK293T cells transiently transfected with human APN R741G (Figures 5A and 5B), lending further support to the importance of the oligosaccharide at position N739 for receptor activity. The human APN R741T oligosaccharide knockin mutant and N741G mutant remained functional as
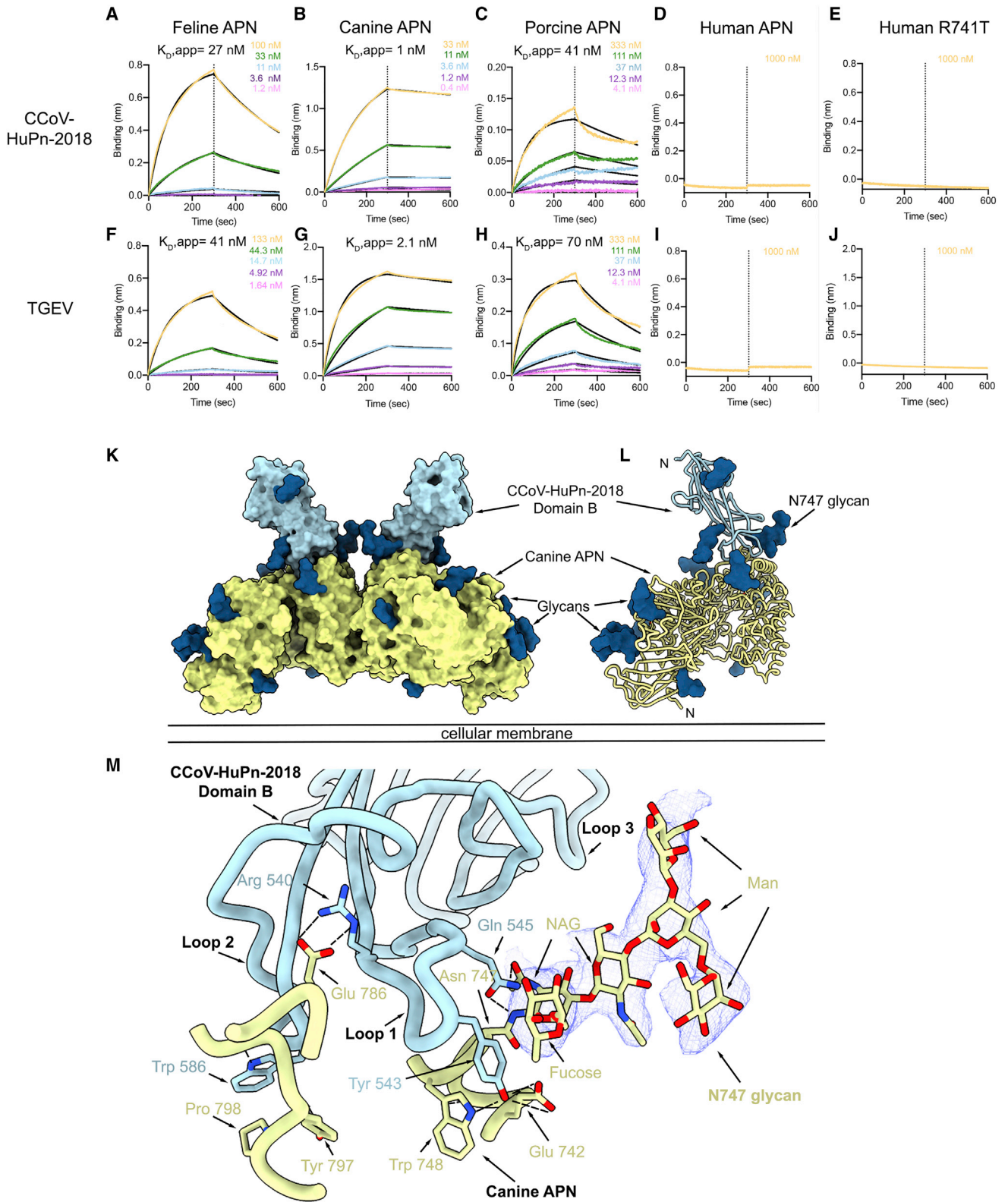
(legend on next page)

demonstrated by the retained interactions with the HCoV-229E B domain (Figures S5G and S5H) and the ability to support 229E S-mediated entry into HEK293T cells (Figure 5C) due to the distal location of the N739 oligosaccharide from the HCoV-229E attachment site (Wong et al., 2017). Binding of CCoV-HuPn-2018 or TGEV B domains to R741T human APN was, however, undetectable using biolayer interferometry (Figures 4E and 4J) or pull-down assays (Figures S5A and S5B), underscoring the low affinity of these interactions. Multivalent display of CCoV-HuPn-2018 S domain B, but not domain 0, at the surface of the I53-50 NP enabled detection of very weak interactions with human R741T APN, relative to canine APN, immobilized at the surface of biolayer interferometry biosensors (Figures S5I and S5J). Collectively, these data demonstrate that multiple APN orthologs are entry receptors for CCoV-HuPn-2018 S-mediated entry into target cells and suggest that the presence of a glycan at position N739 (human APN numbering) is a key factor for entry.

Antigenicity of the CCoV-HuPn-2018 S trimer

CCoV-HuPn-2018 S shares 47% amino acid sequence identity with HCoV-229E S and with HCoV-NL63 S and is therefore more distantly related to the S glycoproteins of these two endemic human-infecting α-coronaviruses than they are to each other (64% sequence identity). Mapping sequence conservation between these three viruses on the CCoV-HuPn-2018 S trimer structure shows that the S_1 subunit is more divergent than the S_2 subunit (Figures 6A and 6B), a trend which holds true across all coronaviruses as a result of differential receptor usage and immune pressure (Pinto et al., 2021; Sauer et al., 2021; Tortorici and Veesler, 2019; Walls et al., 2016a, 2020a).

To investigate the CCoV-HuPn-2018 cross-neutralization afforded by prior α-coronavirus exposure, we evaluated the neutralizing activity of human plasma obtained between 1985 and 1987 from individuals infected with HCoV-229E (Eguia et al., 2021). We observed that plasma inhibiting HCoV-229E-S-mediated entry into cells also blocked CCoV-HuPn-2018 S pseudovirus entry, albeit with reduced potency (Figures 6C, 6D, and S7A–S7C). In contrast, TGEV-S-mediated entry was little affected by any plasma tested (Figures 6E and S7A–S7C). These findings suggest that α-coronavirus infection in humans elicit polyclonal antibody responses with some degree of neutralization breadth toward other coronaviruses in the same genera.

We subsequently evaluated the ability of the previously described PRCV/TGEV 1AF10 neutralizing monoclonal antibody (Wong et al., 2017) to cross-react with the CCoV-HuPn-2018 B domain. Biolayer interferometry measurements showed that the 1AF10 Fab fragment bound to the immobilized CCoV-HuPn-2018 B domain with an affinity of 17 nM with similar on and off rates than those observed for binding to the TGEV B domain (Figures S7D and S7E). Moreover, the 1AF10 Fab potently inhibited CCoV-HuPn-2018 S and TGEV S pseudovirus entry into HEK293T cells transiently transfected with canine, feline, porcine, and human APN N739 oligosaccharide knockin mutant (R741T) (Figures 6F and 6G). We also demonstrated that 1AF10 inhibits APN binding to both the CCoV-HuPn-2018 and the TGEV B domains competitively, indicating that this mAb prevents viral attachment to the host cell surface and might be a suitable therapeutic candidate against CCoV-HuPn-2018 (Figures 6H and 6I).

DISCUSSION

As is the case for several other α-coronaviruses, CCoV-HuPn-2018 S interacts with cell surface carbohydrates (Krempl et al., 1997; Milewska et al., 2014; Regan and Whittaker, 2008; Regan et al., 2010). We suggest that the two S snapshots we captured using cryo-EM correspond to two functionally distinct conformations at various stages of the entry process. These structural changes would couple domain 0 adsorption to host cell surface sialoglycans to subsequent exposure of the B domain to interact with the APN entry receptor. Subsequent protease-mediated cleavage at the S_2' site would activate S for membrane fusion and enable initiation of infection. As similar conformational changes were detected for PEDV S, which also binds glycans using domain 0 (Kirchdoerfer et al., 2021; Wrapp and McLellan, 2019), we propose that this cascade of conformational changes might be conserved among several α-coronaviruses.

We previously described that HCoV-NL63 S domain A N358 glycan participates in obstructing the B domain receptor-binding loops from the same protomer as a putative immune evasion strategy (Walls et al., 2016b; Figure S8A). The CCoV-HuPn-2018 S domain A glycan at position N404 and the domain B glycan at position N561 shield the receptor-binding loops from the same and from a neighboring B domain (to a different extent in the domain 0 proximal and swung-out conformations), respectively (Figures S8B and S8C), and they may play a similar role for this virus. Both CCoV-HuPn-2018 S and HCoV-NL63 S therefore appear to utilize conformational masking and glycan shielding to limit exposure of the receptor-binding loops and possibly reduce recognition by neutralizing antibodies (Reguera et al., 2012; Walls et al., 2016b; Wong et al., 2017).

The ongoing SARS-CoV-2 genetic drift has led to the emergence of variants harboring numerous mutations, especially in the N-terminal domain (domain A) and the receptor-binding

Figure 4. The CCoV-HuPn-2018 S B domain recognizes APN

(A–J) Biolayer interferometry kinetic analysis of feline (A and F), canine (B and G), porcine (C and H), human (D and I), and human R741T (E and J) dimeric APN ectodomains binding to biotinylated CCoV-HuPn-2018 B domain (A–E) or TGEV B domain (F–J) immobilized at the surface of SA biosensors.

(K–L) Surface representation (K) and ribbon diagram (L) of the crystal structure of CCoV-HuPn-2018 B domain (light blue) in complex with the canine APN ectodomain (light yellow). The observed crystallographic dimer is depicted in its likely orientation relative to the plasma membrane in (K). N-linked glycans are depicted as dark blue surfaces.

(M) Close-up view showing key interactions formed between CCoV-HuPn-2018 B domain and the canine APN ectodomain. Dashed lines show salt bridges and hydrogen bonds. The 2Fo-Fc electron density around the N747 glycan is shown as a blue mesh.

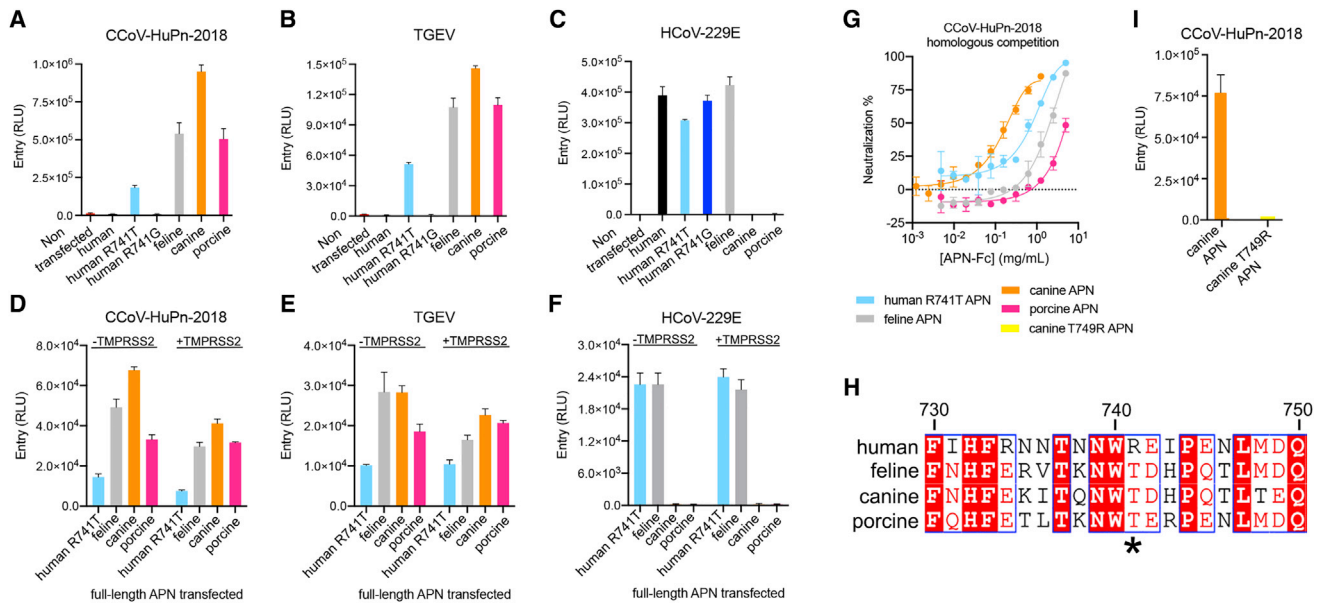See also Figures S3 and S5 and Tables S3 and S4.

Figure 5. APN is a functional entry receptor for CCoV-HuPn-2018

(A–C) Entry of VSV particles pseudotyped with CCoV-HuPn-2018 S (A), TGEV S (B), or HCoV-229E S (C) in HEK293T cells transiently transfected with human, human R741T (glycan knockin), human R741G, feline, canine, or porcine APN orthologs. RLUs, relative luciferase units.

(D–F) Entry of VSV particles pseudotyped with CCoV-HuPn-2018 S (D), TGEV S (E), and HCoV-V229E S (F) in HEK293T cells transiently transfected with human R741T (glycan knockin), canine, feline, or porcine APN orthologs in the presence or absence of TMPRSS2.

(G) Concentration-dependent inhibition of CCoV-HuPn-2018 S pseudovirus entry in HEK293T cells transiently transfected with full-length APN orthologs with matched, purified dimeric soluble APN-Fc ectodomains.

(H) Sequence alignment of human, feline, canine, and porcine APNs focused on the N739 glycosylation sequon. Human APN position 741 is indicated with an asterisk. Residue numbering corresponds to human APN.

(I) Entry of VSV particles pseudotyped with CCoV-HuPn-2018 S in HEK293T cells transiently transfected with canine or canine T749R glycan knockout mutant (equivalent to human APN position 741).

Mean and standard deviation of technical duplicates are graphed. See also Figures S3, S5, and S6 and Tables S3 and S4.

domain (domain B) (Cameroni et al., 2022; Collier et al., 2021; Davies et al., 2021; Deng et al., 2021; Faria et al., 2021; McCallum et al., 2021a, 2021b, 2021c, 2022; Tegally et al., 2021; Thomson et al., 2021). Many of these variants exhibit altered transmissibility, immune evasion, replication kinetics, or disease severity relative to the ancestral SARS-CoV-2 strain (Cele et al., 2021; Collier et al., 2021; Davies et al., 2021; Edara et al., 2021; Liu et al., 2021a, 2021b; McCallum et al., 2021a, 2021b; Meng et al., 2022; Plante et al., 2021; Wibmer et al., 2021). Similarly, a longitudinal survey of HCoV-229E isolates revealed that the (B domain) receptor-binding loops evolve rapidly relative to the rest of the genome resulting in changes in receptor-binding affinity and antigenicity (Wong et al., 2017). This antigenic drift results in dampened plasma neutralization titers of HCoV-229E isolates that have emerged several years after infection (Eguia et al., 2021). Nevertheless, the existence in HCoV-229E patient plasma of cross-reactive Abs with detectable neutralizing activity against CCoV-HuPn-2018 suggests that these antibodies have the potential to reduce disease severity of this virus in humans.

Single-nucleotide polymorphisms of the APN gene (*ANPEP*) have been previously described in humans (Vijgen et al., 2004) and pigs (Bovo et al., 2021), and we identified a rare R741G-carrying allele in a heterozygous individual in public databases (STAR Methods), which does not, however, introduce a glycosylation sequon. Moreover, we observed a near-perfect sequence

conservation of the CCoV-HuPn-2018 receptor-binding loops with those of TGEV/PRCV, although they are distinct viruses. Collectively, these data along with the failure of CCoV-HuPn-2018 S to utilize wild-type human APN and its isolation using canine A72 cells (Vlasova et al., 2021) suggest that CCoV-HuPn-2018 is not well adapted for infection and replication in human hosts. These findings also suggest that subjects infected with this novel virus or with related canine and feline coronaviruses (Lednicky et al., 2021a; Silva and Mullis, 2014; Vlasova et al., 2021) might harbor *ANPEP* variants introducing an oligosaccharide at position N739, which we have shown to enable CCoV-HuPn-2018 S-mediated entry. The rarity of these single-nucleotide polymorphisms is expected to restrict the zoonotic potential of CCoV-HuPn-2018 to a small number of individuals in the absence of further viral adaptations.

The detection of viruses genetically related to canine and feline coronaviruses, including CCoV-HuPn-2018, in humans across two different continents revealed that cross-species transmission of α-coronavirus-1 species, which were not previously known to infect humans, might occur recurrently (Lednicky et al., 2021a; Silva and Mullis, 2014; Vlasova et al., 2021; Xiu et al., 2020). Moreover, demonstration of the ability of porcine deltacoronavirus to use human APN for cell entry and identification of multiple zoonotic transmission events in children in Haiti add an additional coronavirus to the growing list of emerging
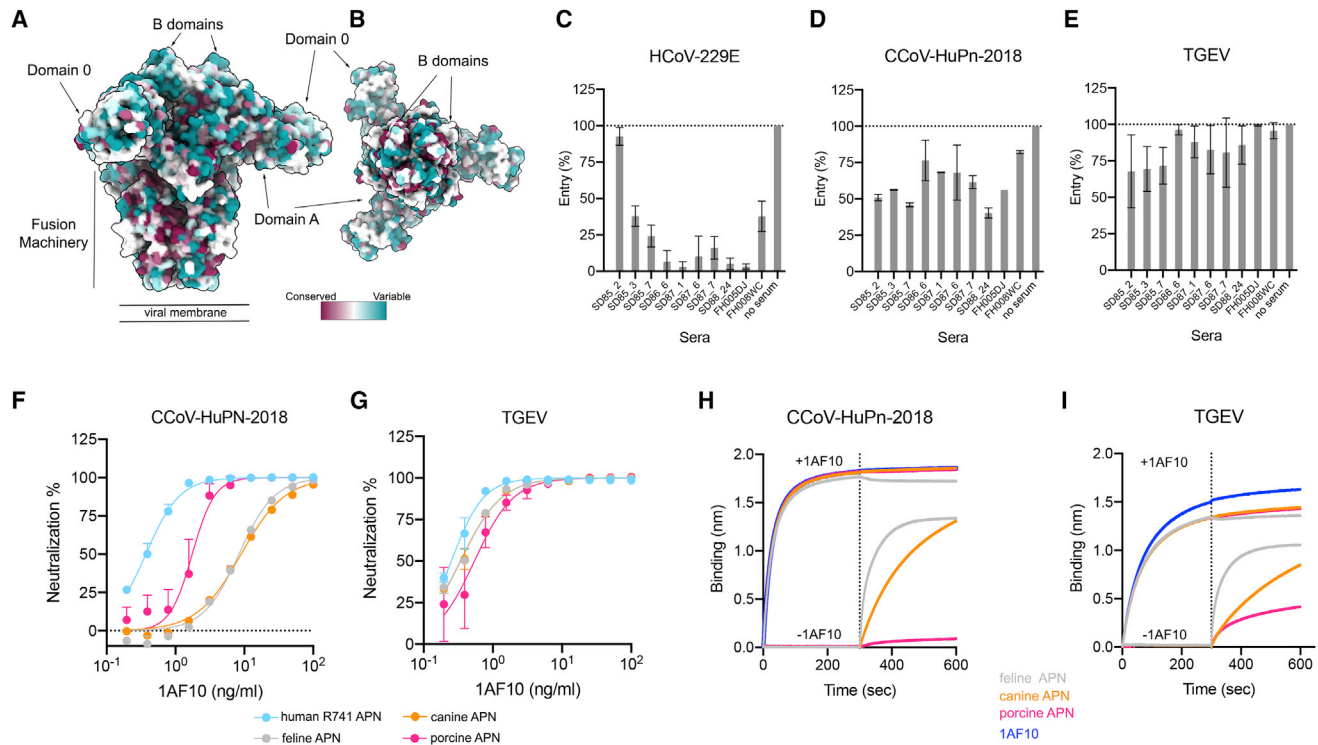
Figure 6. Evaluation of polyclonal and monoclonal antibody neutralization of CCoV-HuPn-2018 S-mediated entry into cells

(A and B) Sequence conservation of HCoV-229E, HCoV-NL63, and CCoV-HuPn-2018 S glycoproteins plotted on the CCoV-HuPn-2018 S structure viewed from the side (A) and top (B). The sequence alignment was generated using the following sequences: CCoV-HuPn-2018 S (QVL91811.1), HCoV-229E S (AAK32191.1 and ABB90515), and HCoV-NL63 S (AIW52835.1 and YP_003767.1). Renderings in (A) and (B) use a composite model obtained from the global and local refinements.

(C–E) HCoV-229E S (C), CCoV-HuPn-2018 S (D), and TGEV S (E) pseudotyped VSV entry in the presence of a 1:5-diluted plasma obtained between 1985 and 1987 from human subjects previously infected with HCoV-229E (dose-response neutralization curves are shown in Figure S7).

(F and G) CCoV-HuPn-2018 S (F) and TGEV S (G) pseudotyped VSV entry in the presence of various concentrations of 1AF10 neutralizing monoclonal Fab fragment in HEK293T cells transfected with the indicated full-length APN orthologs.

(H and I) Competition between 1AF10 Fab and APN for binding to immobilized CoV-HuPn-2018 (H) or TGEV (I) B domains analyzed by biolayer interferometry. Each CoV-HuPn-2018 (H) or TGEV (I) B-domain-loaded SA biosensor was sequentially dipped in a solution containing the 1AF10 Fab at a concentration ten times above the respective affinity (170 nM for CoV-HuPn-2018 or 100 nM for TGEV), and then a solution containing the same concentration of 1AF10 supplemented with canine APN (orange, 10 nM for CoV-HuPn-2018 or 21 nM for TGEV), feline APN (gray, 270 nM for CoV-HuPn-2018 or 470nM for TGEV), porcine APN (pink, 410 nM for CoV-HuPn-2018 or 700 nM for TGEV), or no APN (blue). APNs used here had the Fc tag cleaved.

Mean and standard deviation of technical duplicates are graphed. See also Figure S7.

human pathogens (Lednicky et al., 2021b; Li et al., 2018). Finally, the recent identification of bat merbecoviruses able to utilize ACE2 as entry receptor underscores the promiscuity of these viruses and their pandemic potential (Xiong et al., 2022). The data presented here along with continued surveillance and characterization of emerging coronaviruses will support pandemic preparedness efforts similar to prior work that enabled a rapid response to the COVID-19 pandemic.

Limitations of the study

We showed that canine, feline, and porcine APN orthologs promote CCoV-HuPn-2018-S-mediated entry into cells and that the glycan at position N747 of canine APN is critical for entry. Human APN can serve as entry receptor only if a glycan is introduced at the equivalent position (N739). Although APN single-nucleotide polymorphisms have been documented in humans, none of them introduce an N-linked glycosylation sequon at this position.

Further studies will be needed to elucidate whether individuals infected with CCoV-HuPn-2018 harbor such single-nucleotide polymorphisms.

STAR★METHODS

Detailed methods are provided in the online version of this paper and include the following:

- KEY RESOURCES TABLE
- RESOURCE AVAILABILITY
  - Lead contact
  - Materials availability
  - Data and code availability
- EXPERIMENTAL MODEL AND SUBJECT DETAILS
  - Cell lines
  - Plasmids

- Mutagenesis
- Protein expression and purification
- Protein biotinylation
- Biolayer interferometry
- Pull-down assays
- Bacterial protein expression and purification of nano-particles components
- *In vitro* nanoparticle assembly
- Negative stain electron microscopy
- Hemagglutination assays
- VSV pseudotyped virus production
- Pseudotyped VSV infections and neutralizations
- Western blot
- Crystallization, data collection, structure determination and analysis
- CryoEM sample preparation, data collection and data processing
- CryoEM model building and analysis
- Assessment of human *ANPEP* diversity

SUPPLEMENTAL INFORMATION

Supplemental information can be found online at https://doi.org/10.1016/j.cell.2022.05.019.

AUTHOR CONTRIBUTIONS

M.A.T. and D.V. conceived the project. M.A.T., A.C.W., and D.V. designed experiments. A.C.W. and A.J. performed BLI binding assays. M.A.T. performed site-directed mutagenesis. M.A.T. and A.J. carried out pull-down assays. M.A.T. ran pseudotyped virus entry assays. M.A.T. and A.J. expressed and purified the recombinant proteins. M.C.M. and A.D. prepared HKU1-S and HA-ferritin NPs. M.A.T performed hemagglutination assays. M.A.T. and Y.J.P. collected the cryo-EM data. M.A.T. processed the cryo-EM data. M.A.T. and D.V. built and refined the atomic models. M.A.T. performed crystallization, X-ray data collection, and structure determination. M.A.T. and D.V. refined the crystal structure. A.T. performed the SNP analysis. R.T.E., T.S.-A., M.J.B., A.L., D.C., N.P.K., and J.D.B. provided unique reagents. M.A.T. and D.V. wrote the manuscript with input from all authors.

DECLARATION OF INTERESTS

A.T., A.L., and D.C. are employees of Vir Biotechnology Inc. and may hold shares in Vir Biotechnology Inc. D.C. is currently listed as an inventor on multiple patent applications, which disclose the subject matter described in this manuscript. The Veesler laboratory has received a sponsored research agreement from Vir Biotechnology Inc. The remaining authors declare that the research was conducted in the absence of any commercial or financial relationships that could be construed as a potential conflict of interests.

REFERENCES

Agirre, J., Iglesias-Fernández, J., Rovira, C., Davies, G.J., Wilson, K.S., and Cowtan, K.D. (2015). Privateer: software for the conformational validation of carbohydrate structures. Nat. Struct. Mol. Biol. *22*, 833–834.

Anthony, S.J., Gilardi, K., Menachery, V.D., Goldstein, T., Ssebide, B., Mbabazi, R., Navarrete-Macias, I., Liang, E., Wells, H., Hicks, A., et al. (2017). Further evidence for bats as the evolutionary source of Middle East respiratory syndrome coronavirus. mBio *8*. e00373–e00317.

Armon, A., Graur, D., and Ben-Tal, N. (2001). ConSurf: an algorithmic tool for the identification of functional regions in proteins by surface mapping of phylogenetic information. Journal of Molecular Biology *307*, 447–463.

Arunachalam, P.S., Walls, A.C., Golden, N., Atyeo, C., Fischinger, S., Li, C., Aye, P., Navarro, M.J., Lai, L., Edara, V.V., et al. (2021). Adjuvanting a subunit COVID-19 vaccine to induce protective immunity. Nature *594*, 253–258.

Bale, J.B., Gonen, S., Liu, Y., Sheffler, W., Ellis, D., Thomas, C., Cascio, D., Yeates, T.O., Gonen, T., King, N.P., et al. (2016). Accurate design of megadalton-scale two-component icosahedral protein complexes. Science *353*, 389–394.

Baum, A., Fulton, B.O., Wloga, E., Copin, R., Pascal, K.E., Russo, V., Giordano, S., Lanza, K., Negron, N., Ni, M., et al. (2020). Antibody cocktail to SARS-CoV-2 spike protein prevents rapid mutational escape seen with individual antibodies. Science *369*, 1014–1018.

Bertram, S., Dijkman, R., Habjan, M., Heurich, A., Gierer, S., Glowacka, I., Welsch, K., Winkler, M., Schneider, H., Hofmann-Winkler, H., et al. (2013). TMPRSS2 activates the human coronavirus 229E for cathepsin-independent host cell entry and is expressed in viral target cells in the respiratory epithelium. J. Virol. *87*, 6150–6160.

Bond, C.S. (2003). TopDraw: a sketchpad for protein structure topology cartoons. Bioinformatics *19*, 311–312.

Bovo, S., Schiavo, G., Ribani, A., Utzeri, V.J., Taurisano, V., Ballan, M., Muñoz, M., Alves, E., Araujo, J.P., Bozzi, R., et al. (2021). Describing variability in pig genes involved in coronavirus infections for a One Health perspective in conservation of animal genetic resources. Sci. Rep. *11*, 3359.

Cameroni, E., Bowen, J.E., Rosen, L.E., Saliba, C., Zepeda, S.K., Culap, K., Pinto, D., VanBlargan, L.A., De Marco, A., di Iulio, J., et al. (2022). Broadly neutralizing antibodies overcome SARS-CoV-2 Omicron antigenic shift. Nature *602*, 664–670.

Cele, S., Gazy, I., Jackson, L., Hwa, S.-H., Tegally, H., Lustig, G., Giandhari, J., Pillay, S., Wilkinson, E., Naidoo, Y., et al. (2021). Escape of SARS-CoV-2 501y.V2 from Neutralization by Convalescent Plasma (Nature Publishing).

Chen, S., McMullan, G., Faruqi, A.R., Murshudov, G.N., Short, J.M., Scheres, S.H., and Henderson, R. (2013). High-resolution noise substitution to measure overfitting and validate resolution in 3D structure determination by single particle electron cryomicroscopy. Ultramicroscopy *135*, 24–35.

Chen, V.B., Arendall, W.B., Headd, J.J., Keedy, D.A., Immormino, R.M., Kapral, G.J., Murray, L.W., Richardson, J.S., and Richardson, D.C. (2010). MolProbity: all-atom structure validation for macromolecular crystallography. Acta Crystallogr. D Biol. Crystallogr. *66*, 12–21.

Collier, D.A., De Marco, A., Ferreira, I.A.T.M., Meng, B., Datir, R.P., Walls, A.C., Kemp, S.A., Bassi, J., Pinto, D., Silacci-Fregni, C., et al. (2021). Sensitivity of SARS-CoV-2 B.1.1.7 to mRNA vaccine-elicited antibodies. Nature *593*, 136–141.

Corbett, K.S., Edwards, D.K., Leist, S.R., Abiona, O.M., Boyoglu-Barnum, S., Gillespie, R.A., Himansu, S., Schäfer, A., Ziwawo, C.T., DiPiazza, A.T., et al.

(2020). SARS-CoV-2 mRNA vaccine design enabled by prototype pathogen preparedness. Nature *586*, 567–571.

Corti, D., Purcell, L.A., Snell, G., and Veesler, D. (2021). Tackling COVID-19 with neutralizing monoclonal antibodies. Cell *184*, 3086–3108.

Davies, N.G., Abbott, S., Barnard, R.C., Jarvis, C.I., Kucharski, A.J., Munday, J.D., Pearson, C.A.B., Russell, T.W., Tully, D.C., Washburne, A.D., et al. (2021). Estimated transmissibility and impact of SARS-CoV-2 lineage B.1.1.7 in England. Science *372*, eabg3055.

Delaune, D., Hul, V., Karlsson, E.A., Hassanin, A., Ou, T.P., Baidaliuk, A., Gámbaro, F., Prot, M., Tu, V.T., Chea, S., et al. (2021). A novel SARS-CoV-2 related coronavirus in bats from Cambodia. Nat. Commun. *12*, 6563.

Delmas, B., Gelfi, J., L'Haridon, R., Vogel, L.K., Sjöström, H., Norén, O., and Laude, H. (1992). Aminopeptidase N is a major receptor for the enteropathogenic coronavirus TGEV. Nature *357*, 417–420.

Deng, X., Garcia-Knight, M.A., Khalid, M.M., Servellita, V., Wang, C., Morris, M.K., Sotomayor-González, A., Glasner, D.R., Reyes, K.R., Gliwa, A.S., et al. (2021). Transmission, infectivity, and neutralization of a spike L452R SARS-CoV-2 variant. Cell *184*, 3426–3437.e8.

Edara, V.-V., Pinsky, B.A., Suthar, M.S., Lai, L., Davis-Gardner, M.E., Floyd, K., Flowers, M.W., Wrammert, J., Hussaini, L., Ciric, C.R., et al. (2021). Infection and vaccine-induced neutralizing-antibody responses to the SARS-CoV-2 B.1.617 Variants. N. Engl. J. Med. *385*, 664–666.

Eguia, R.T., Crawford, K.H.D., Stevens-Ayers, T., Kelnhofer-Millevolte, L., Greninger, A.L., Englund, J.A., Boeckh, M.J., and Bloom, J.D. (2021). A human coronavirus evolves antigenically to escape antibody immunity. PLoS Pathog. *17*, e1009453.

Emsley, P., Lohkamp, B., Scott, W.G., and Cowtan, K. (2010). Features and development of coot. Acta Crystallogr. D Biol. Crystallogr. *66*, 486–501.

Emsley, P., Lohkamp, B., Scott, W.G., and Cowtan, K. (2010). Features and development of *Coot*. Acta Cryst. *D66*, 486–501.

Faria, N.R., Mellan, T.A., Whittaker, C., Claro, I.M., Candido, D.D.S., Mishra, S., Crispim, M.A.E., Sales, F.C.S., Hawryluk, I., McCrone, J.T., et al. (2021). Genomics and epidemiology of the P.1 SARS-CoV-2 lineage in Manaus, Brazil. Science *372*, 815–821.

Frenz, B., Rämisch, S., Borst, A.J., Walls, A.C., Adolf-Bryfogle, J., Schief, W.R., Veesler, D., and DiMaio, F. (2019). Automatically fixing errors in glycoprotein structures with Rosetta. Structure *27*, 134–139.e3.

Goddard, T.D., Huang, C.C., Meng, E.C., Pettersen, E.F., Couch, G.S., Morris, J.H., and Ferrin, T.E. (2018). UCSF ChimeraX: meeting modern challenges in visualization and analysis. Protein Sci. *27*, 14–25.

Hansen, J., Baum, A., Pascal, K.E., Russo, V., Giordano, S., Wloga, E., Fulton, B.O., Yan, Y., Koon, K., Patel, K., et al. (2020). Studies in humanized mice and convalescent humans yield a SARS-CoV-2 antibody cocktail. Science *369*, 1010–1014.

Hsu, S.T.D., Yang, T.J., Ko, T.P., and Draczkowski, P. (2020). Cryo-EM structure of spike protein of feline infectious peritonitis virus strain UU4. Proc Natl Acad Sci USA *117*, 1438–1446.

Hulswit, R.J.G., Lang, Y., Bakkers, M.J.G., Li, W., Li, Z., Schouten, A., Ophorst, B., van Kuppeveld, F.J.M., Boons, G.J., Bosch, B.J., et al. (2019). Human coronaviruses OC43 and HKU1 bind to 9-O-acetylated sialic acids via a conserved receptor-binding site in spike protein domain A. Proc. Natl. Acad. Sci. USA *116*, 2681–2690.

Kabsch, W. (2010). XDS. Acta Crystallogr. D Biol. Crystallogr. *66*, 125–132.

Kaname, Y., Tani, H., Kataoka, C., Shiokawa, M., Taguwa, S., Abe, T., Moriishi, K., Kinoshita, T., and Matsuura, Y. (2010). Acquisition of complement resistance through incorporation of CD55/decay-accelerating factor into viral particles bearing baculovirus gp64. J. Virol. *84*, 3210–3219.

Kanekiyo, M., Wei, C.-J., Yassine, H.M., McTamney, P.M., Boyington, J.C., Whittle, J.R.R., Rao, S.S., Kong, W.-P., Wang, L., and Nabel, G.J. (2013). Self-assembling influenza nanoparticle vaccines elicit broadly neutralizing H1N1 antibodies. Nature *499*, 102–106.

Kirchdoerfer, R.N., Bhandari, M., Martini, O., Sewall, L.M., Bangaru, S., Yoon, K.-J., and Ward, A.B. (2021). Structure and immune recognition of the porcine epidemic diarrhea virus spike protein. Structure *29*, 385–392.e5.

Krempl, C., Schultze, B., Laude, H., and Herrler, G. (1997). Point mutations in the S protein connect the sialic acid binding activity with the enteropathogenicity of transmissible gastroenteritis coronavirus. J. Virol. *71*, 3285–3287.

Lednicky, J.A., Tagliamonte, M.S., White, S.K., Blohm, G.M., Alam, M.M., Iovine, N.M., Salemi, M., Mavian, C., and Morris, J.G. (2021a). Isolation of a novel recombinant canine coronavirus from a visitor to Haiti: further evidence of transmission of coronaviruses of zoonotic origin to humans. Clin. Infect. Dis. https://doi.org/10.1093/cid/ciab924.

Lednicky, J.A., Tagliamonte, M.S., White, S.K., Elbadry, M.A., Alam, M.M., Stephenson, C.J., Bonny, T.S., Loeb, J.C., Telisma, T., Chavannes, S., et al. (2021b). Emergence of porcine delta-coronavirus pathogenic infections among children in Haiti through independent zoonoses and convergent evolution. Preprint at medRxiv. https://doi.org/10.1101/2021.03.19.21253391.

Lempp, F.A., Soriaga, L., Montiel-Ruiz, M., Benigni, F., Noack, J., Park, Y.-J., Bianchi, S., Walls, A.C., Bowen, J.E., Zhou, J., et al. (2021). Membrane lectins enhance SARS-CoV-2 infection and influence the neutralizing activity of different classes of antibodies. Preprint at bioRxiv. https://doi.org/10.1101/2021.04.03.438258.

Li, W., Hulswit, R.J.G., Kenney, S.P., Widjaja, I., Jung, K., Alhamo, M.A., van Dieren, B., van Kuppeveld, F.J.M., Saif, L.J., and Bosch, B.J. (2018). Broad receptor engagement of an emerging global coronavirus may potentiate its diverse cross-species transmissibility. Proc. Natl. Acad. Sci. USA *115*, E5135–E5143.

Li, W., Hulswit, R.J.G., Widjaja, I., Raj, V.S., McBride, R., Peng, W., Widagdo, W., Tortorici, M.A., van Dieren, B., Lang, Y., et al. (2017). Identification of sialic acid-binding function for the Middle East respiratory syndrome coronavirus spike glycoprotein. Proc. Natl. Acad. Sci. USA *114*, E8508–E8517.

Li, Z., Tomlinson, A.C., Wong, A.H., Zhou, D., Desforges, M., Talbot, P.J., Benlekbir, S., Rubinstein, J.L., and Rini, J.M. (2019). The human coronavirus HCoV-229E S-protein structure and receptor binding. Elife *8*, e51230.

Licitra, B.N., Millet, J.K., Regan, A.D., Hamilton, B.S., Rinaldi, V.D., Duhamel, G.E., and Whittaker, G.R. (2013). Mutation in spike protein cleavage site and pathogenesis of feline coronavirus. Emerg. Infect. Dis. *19*, 1066–1073.

Liebschner, D., Afonine, P.V., Baker, M.L., Bunkóczi, G., Chen, V.B., Croll, T.I., Hintze, B., Hung, L.W., Jain, S., McCoy, A.J., et al. (2019). Macromolecular structure determination using X-rays, neutrons and electrons: recent developments in Phenix. Acta Crystallogr. D Struct. Biol. *75*, 861–877.

Liebschner, D., Afonine, P.V., Baker, M.L., Bunkóczi, G., Chen, V.B., Croll, T.I., Hintze, B., Hung, L.-W., Jain, S., McCoy, A.J., et al. (2019). Macromolecular structure determination using X-rays, neutrons and electrons: recent developments in *Phenix*. Acta Cryst *D75*, 861–877.

Liu, C., Ginn, H.M., Dejnirattisai, W., Supasa, P., Wang, B., Tuekprakhon, A., Nutalai, R., Zhou, D., Mentzer, A.J., Zhao, Y., et al. (2021a). Reduced neutralization of SARS-CoV-2 B.1.617 by vaccine and convalescent serum. Cell *184*, 4220–4236.e13.

Liu, Y., Liu, J., Johnson, B.A., Xia, H., Ku, Z., Schindewolf, C., Widen, S.G., An, Z., Weaver, S.C., Menachery, V.D., et al. (2021b). Delta spike P681R mutation enhances SARS-CoV-2 fitness over Alpha variant. Preprint at bioRxiv. https://doi.org/10.1101/2021.08.12.456173.

Lu, G., Hu, Y., Wang, Q., Qi, J., Gao, F., Li, Y., Zhang, Y., Zhang, W., Yuan, Y., Bao, J., et al. (2013). Molecular basis of binding between novel human coronavirus MERS-CoV and its receptor CD26. Nature *500*, 227–231.

McCallum, M., Bassi, J., De Marco, A., Chen, A., Walls, A.C., Di Iulio, J., Tortorici, M.A., Navarro, M.-J., Silacci-Fregni, C., Saliba, C., et al. (2021b). SARS-CoV-2 immune evasion by the B.1.427/B.1.429 variant of concern. Science *373*, 648–654.

McCallum, M., Czudnochowski, N., Rosen, L.E., Zepeda, S.K., Bowen, J.E., Walls, A.C., Hauser, K., Joshi, A., Stewart, C., Dillen, J.R., et al. (2022). Structural basis of SARS-CoV-2 Omicron immune evasion and receptor engagement. Science *375*, eabn8652.

McCallum, M., De Marco, A., Lempp, F.A., Tortorici, M.A., Pinto, D., Walls, A.C., Beltramello, M., Chen, A., Liu, Z., Zatta, F., et al. (2021a). N-terminal domain antigenic mapping reveals a site of vulnerability for SARS-CoV-2. Cell 184, 2332–2347.e16.

McCallum, M., Walls, A.C., Sprouse, K.R., Bowen, J.E., Rosen, L.E., Dang, H.V., De Marco, A., Franko, N., Tilles, S.W., Logue, J., et al. (2021c). Molecular basis of immune evasion by the Delta and Kappa SARS-CoV-2 variants. Science 374, 1621–1626.

McCoy, A.J., Grosse-Kunstleve, R.W., Adams, P.D., Winn, M.D., Storoni, L.C., and Read, R.J. (2007). Phaser crystallographic software. J. Appl. Crystallogr. 40, 658–674.

Menachery, V.D., Dinnon, K.H., Yount, B.L., McAnarney, E.T., Gralinski, L.E., Hale, A., Graham, R.L., Scobey, T., Anthony, S.J., Wang, L., et al. (2020). Trypsin treatment unlocks barrier for zoonotic bat coronavirus infection. J. Virol. 94. e01774–e01719.

Menachery, V.D., Yount, B.L., Debbink, K., Agnihothram, S., Gralinski, L.E., Plante, J.A., Graham, R.L., Scobey, T., Ge, X.Y., Donaldson, E.F., et al. (2015). A SARS-like cluster of circulating bat coronaviruses shows potential for human emergence. Nat. Med. 21, 1508–1513.

Menachery, V.D., Yount, B.L., Sims, A.C., Debbink, K., Agnihothram, S.S., Gralinski, L.E., Graham, R.L., Scobey, T., Plante, J.A., Royal, S.R., et al. (2016). SARS-like WIV1-CoV poised for human emergence. Proc. Natl. Acad. Sci. USA 113, 3048–3053.

Meng, B., Abdullahi, A., Ferreira, I.A.T.M., Goonawardane, N., Saito, A., Kimura, I., Yamasoba, D., Gerber, P.P., Fatihi, S., Rathore, S., et al. (2022). Altered TMPRSS2 usage by SARS-CoV-2 Omicron impacts tropism and fusogenicity. Nature 603, 706–714.

Milewska, A., Zarebski, M., Nowak, P., Stozek, K., Potempa, J., and Pyrc, K. (2014). Human coronavirus NL63 utilizes heparan sulfate proteoglycans for attachment to target cells. J. Virol. 88, 13221–13230.

Millet, J.K., and Whittaker, G.R. (2014). Host cell entry of Middle East respiratory syndrome coronavirus after two-step, furin-mediated activation of the spike protein. Proc. Natl. Acad. Sci. USA 111, 15214–15219.

Millet, J.K., and Whittaker, G.R. (2015). Host cell proteases: critical determinants of coronavirus tropism and pathogenesis. Virus Res. 202, 120–134.

Pallesen, J., Wang, N., Corbett, K.S., Wrapp, D., Kirchdoerfer, R.N., Turner, H.L., Cottrell, C.A., Becker, M.M., Wang, L., Shi, W., et al. (2017). Immunogenicity and structures of a rationally designed prefusion MERS-CoV spike antigen. Proc. Natl. Acad. Sci. USA 114, E7348–E7357.

Park, Y.-J., De Marco, A., Starr, T.N., Liu, Z., Pinto, D., Walls, A.C., Zatta, F., Zepeda, S.K., Bowen, J.E., Sprouse, K.R., et al. (2022). Antibody-mediated broad sarbecovirus neutralization through ACE2 molecular mimicry. Science 375, eabm8143.

Park, Y.J., Walls, A.C., Wang, Z., Sauer, M.M., Li, W., Tortorici, M.A., Bosch, B.J., DiMaio, F., and Veesler, D. (2019). Structures of MERS-CoV spike glycoprotein in complex with sialoside attachment receptors. Nat. Struct. Mol. Biol. 26, 1151–1157.

Peng, G., Sun, D., Rajashankar, K.R., Qian, Z., Holmes, K.V., and Li, F. (2011). Crystal structure of mouse coronavirus receptor-binding domain complexed with its murine receptor. Proc. Natl. Acad. Sci. USA 108, 10696–10701.

Pettersen, E.F., Goddard, T.D., Huang, C.C., Couch, G.S., Greenblatt, D.M., Meng, E.C., and Ferrin, T.E. (2004). UCSF Chimera–a visualization system for exploratory research and analysis. J. Comput. Chem. 25, 1605–1612.

Piccoli, L., Park, Y.J., Tortorici, M.A., Czudnochowski, N., Walls, A.C., Beltramello, M., Silacci-Fregni, C., Pinto, D., Rosen, L.E., Bowen, J.E., et al. (2020). Mapping neutralizing and immunodominant sites on the SARS-CoV-2 spike receptor-binding domain by structure-guided high-resolution serology. Cell 183, 1024–1042.e21.

Pinto, D., Park, Y.J., Beltramello, M., Walls, A.C., Tortorici, M.A., Bianchi, S., Jaconi, S., Culap, K., Zatta, F., De Marco, A., et al. (2020). Cross-neutralization of SARS-CoV-2 by a human monoclonal SARS-CoV antibody. Nature 583, 290–295.

Pinto, D., Sauer, M.M., Czudnochowski, N., Low, J.S., Tortorici, M.A., Housley, M.P., Noack, J., Walls, A.C., Bowen, J.E., Guarino, B., et al. (2021). Broad Betacoronavirus neutralization by a stem helix–specific human antibody. Science 373, 1109–1116.

Plante, J.A., Liu, Y., Liu, J., Xia, H., Johnson, B.A., Lokugamage, K.G., Zhang, X., Muruato, A.E., Zou, J., Fontes-Garfias, C.R., et al. (2021). Spike mutation D614G alters SARS-CoV-2 fitness. Nature 592, 116–121.

Polack, F.P., Thomas, S.J., Kitchin, N., Absalon, J., Gurtman, A., Lockhart, S., Perez, J.L., Pérez Marc, G., Moreira, E.D., Zerbini, C., et al. (2020). Safety and efficacy of the BNT162b2 mRNA Covid-19 vaccine. N. Engl. J. Med. 383, 2603–2615.

Punjani, A., Rubinstein, J.L., Fleet, D.J., and Brubaker, M.A. (2017). cryoSPARC: algorithms for rapid unsupervised cryo-EM structure determination. Nat. Methods 14, 290–296.

Punjani, A., Zhang, H., and Fleet, D.J. (2020). Non-uniform refinement: adaptive regularization improves single-particle cryo-EM reconstruction. Nat. Methods 17, 1214–1221.

Regan, A.D., Ousterout, D.G., and Whittaker, G.R. (2010). Feline lectin activity is critical for the cellular entry of feline infectious peritonitis virus. J. Virol. 84, 7917–7921.

Regan, A.D., and Whittaker, G.R. (2008). Utilization of DC-SIGN for entry of feline coronaviruses into host cells. J. Virol. 82, 11992–11996.

Reguera, J., Santiago, C., Mudgal, G., Ordoño, D., Enjuanes, L., and Casasnovas, J.M. (2012). Structural bases of coronavirus attachment to host aminopeptidase N and its inhibition by neutralizing antibodies. PLoS Pathog. 8, e1002859.

Rosenthal, P.B., and Henderson, R. (2003). Optimal determination of particle orientation, absolute hand, and contrast loss in single-particle electron cryomicroscopy. J. Mol. Biol. 333, 721–745.

Sauer, M.M., Tortorici, M.A., Park, Y.-J., Walls, A.C., Homad, L., Acton, O.J., Bowen, J.E., Wang, C., Xiong, X., de van der Schueren, W., et al. (2021). Structural basis for broad coronavirus neutralization. Nat. Struct. Mol. Biol. 28, 478–486.

Shang, J., Zheng, Y., Yang, Y., Liu, C., Geng, Q., Tai, W., Du, L., Zhou, Y., Zhang, W., and Li, F. (2018). Cryo-electron microscopy structure of porcine Deltacoronavirus spike protein in the prefusion state. J. Virol. 92. e01556–e01517.

Silva, C.S., and Mullis, L.B. (2014). Human respiratory coronaviruses detected in patients with InfluenzaLike illness in Arkansas, USA. Virol. Mycol. 01, 004.

Suloway, C., Pulokas, J., Fellmann, D., Cheng, A., Guerra, F., Quispe, J., Stagg, S., Potter, C.S., and Carragher, B. (2005). Automated molecular microscopy: the new Leginon system. J. Struct. Biol. 151, 41–60.

Tegally, H., Wilkinson, E., Giovanetti, M., Iranzadeh, A., Fonseca, V., Giandhari, J., Doolabh, D., Pillay, S., San, E.J., Msomi, N., et al. (2021). Emergence of a SARS-CoV-2 variant of concern with mutations in spike glycoprotein. Nature 592, 438–443.

Tegunov, D., and Cramer, P. (2019). Real-time cryo-electron microscopy data preprocessing with Warp. Nat. Methods 16, 1146–1152.

Thomson, E.C., Rosen, L.E., Shepherd, J.G., Spreafico, R., da Silva Filipe, A., Wojcechowskyj, J.A., Davis, C., Piccoli, L., Pascall, D.J., Dillen, J., et al. (2021). Circulating SARS-CoV-2 spike N439K variants maintain fitness while evading antibody-mediated immunity. Cell 184, 1171–1187.e20.

Tortorici, M.A., Beltramello, M., Lempp, F.A., Pinto, D., Dang, H.V., Rosen, L.E., McCallum, M., Bowen, J., Minola, A., Jaconi, S., et al. (2020). Ultrapotent human antibodies protect against SARS-CoV-2 challenge via multiple mechanisms. Science 370, 950–957.

Tortorici, M.A., Czudnochowski, N., Starr, T.N., Marzi, R., Walls, A.C., Zatta, F., Bowen, J.E., Jaconi, S., Di Iulio, J., Wang, Z., et al. (2021). Broad sarbecovirus neutralization by a human monoclonal antibody. Nature 597, 103–108.

Tortorici, M.A., and Veesler, D. (2019). Structural insights into coronavirus entry. Adv. Virus Res. 105, 93–116.

Tortorici, M.A., Walls, A.C., Lang, Y., Wang, C., Li, Z., Koerhuis, D., Boons, G.J., Bosch, B.J., Rey, F.A., de Groot, R.J., et al. (2019). Structural basis for

human coronavirus attachment to sialic acid receptors. Nat. Struct. Mol. Biol. *26*, 481–489.

Tusell, S.M., Schittone, S.A., and Holmes, K.V. (2007). Mutational analysis of aminopeptidase N, a receptor for several group 1 coronaviruses, identifies key determinants of viral host range. J. Virol. *81*, 1261–1273.

Vijgen, L., Keyaerts, E., Zlateva, K., and Van Ranst, M. (2004). Identification of six new polymorphisms in the human coronavirus 229E receptor gene (aminopeptidase N/CD13). Int. J. Infect. Dis. *8*, 217–222.

Vlasak, R., Luytjes, W., Spaan, W., and Palese, P. (1988). Human and bovine coronaviruses recognize sialic acid-containing receptors similar to those of influenza C viruses. Proc. Natl. Acad. Sci. USA *85*, 4526–4529.

Vlasova, A.N., Diaz, A., Damtie, D., Xiu, L., Toh, T.-H., Lee, J.S.-Y., Saif, L.J., and Gray, G.C. (2021). Novel canine coronavirus isolated from a hospitalized pneumonia patient, East Malaysia. Clin. Infect. Dis. *74*, 446–454.

Walls, A.C., Fiala, B., Schäfer, A., Wrenn, S., Pham, M.N., Murphy, M., Tse, L.V., Shehata, L., O'Connor, M.A., Chen, C., et al. (2020b). Elicitation of potent neutralizing antibody responses by designed protein nanoparticle vaccines for SARS-CoV-2. Cell *183*, 1367–1382.e17.

Walls, A.C., Miranda, M.C., Schäfer, A., Pham, M.N., Greaney, A., Arunachalam, P.S., Navarro, M.-J., Tortorici, M.A., Rogers, K., O'Connor, M.A., et al. (2021). Elicitation of broadly protective sarbecovirus immunity by receptor-binding domain nanoparticle vaccines. Cell *184*, 5432–5447.e16.

Walls, A.C., Park, Y.J., Tortorici, M.A., Wall, A., McGuire, A.T., and Veesler, D. (2020a). Structure, function, and antigenicity of the SARS-CoV-2 spike glycoprotein. Cell *181*, 281–292.e6.

Walls, A.C., Tortorici, M.A., Bosch, B.J., Frenz, B., Rottier, P.J.M., DiMaio, F., Rey, F.A., and Veesler, D. (2016a). Cryo-electron microscopy structure of a coronavirus spike glycoprotein trimer. Nature *531*, 114–117.

Walls, A.C., Tortorici, M.A., Frenz, B., Snijder, J., Li, W., Rey, F.A., DiMaio, F., Bosch, B.J., and Veesler, D. (2016b). Glycan shield and epitope masking of a coronavirus spike protein observed by cryo-electron microscopy. Nat. Struct. Mol. Biol. *23*, 899–905.

Walls, A.C., Tortorici, M.A., Snijder, J., Xiong, X., Bosch, B.J., Rey, F.A., and Veesler, D. (2017). Tectonic conformational changes of a coronavirus spike glycoprotein promote membrane fusion. Proc. Natl. Acad. Sci. USA *114*, 11157–11162.

Walls, A.C., Xiong, X., Park, Y.J., Tortorici, M.A., Snijder, J., Quispe, J., Cameroni, E., Gopal, R., Dai, M., Lanzavecchia, A., et al. (2019). Unexpected receptor functional mimicry elucidates activation of coronavirus fusion. Cell *176*, 1026–1039.e15.

Wang, R.Y., Song, Y., Barad, B.A., Cheng, Y., Fraser, J.S., and DiMaio, F. (2016). Automated structure refinement of macromolecular assemblies from cryo-EM maps using Rosetta. Elife *5*, e17219.

Wibmer, C.K., Ayres, F., Hermanus, T., Madzivhandila, M., Kgagudi, P., Oosthuysen, B., Lambson, B.E., de Oliveira, T., Vermeulen, M., van der Berg, K., et al. (2021). SARS-CoV-2 501Y.V2 escapes neutralization by South African COVID-19 donor plasma. Nat. Med. *27*, 622–625.

Wong, A.H.M., Tomlinson, A.C.A., Zhou, D., Satkunarajah, M., Chen, K., Sharon, C., Desforges, M., Talbot, P.J., and Rini, J.M. (2017). Receptor-binding loops in Alphacoronavirus adaptation and evolution. Nat. Commun. *8*, 1735.

Wrapp, D., and McLellan, J.S. (2019). The 3.1-angstrom cryo-electron microscopy structure of the porcine epidemic diarrhea virus spike protein in the prefusion conformation. J. Virol. *93*. e00923–e00919.

Wu, K., Li, W., Peng, G., and Li, F. (2009). Crystal structure of NL63 respiratory coronavirus receptor-binding domain complexed with its human receptor. Proc. Natl. Acad. Sci. USA *106*, 19970–19974.

Xiong, Q., Cao, L., Ma, C., Liu, C., Si, J., Liu, P., Gu, M., Wang, C., Shi, L., Tong, F., et al. (2022). Close relatives of MERS-CoV in bats use ACE2 as their functional receptors. Preprint at bioRxiv. https://doi.org/10.1101/2022.01.24.477490.

Xiong, X., Tortorici, M.A., Snijder, J., Yoshioka, C., Walls, A.C., Li, W., McGuire, A.T., Rey, F.A., Bosch, B.J., and Veesler, D. (2018). Glycan shield and fusion activation of a Deltacoronavirus Spike glycoprotein fine-tuned for enteric infections. J. Virol. *92*. e01628–e01617.

Xiu, L., Binder, R.A., Alarja, N.A., Kochek, K., Coleman, K.K., Than, S.T., Bailey, E.S., Bui, V.N., Toh, T.-H., Erdman, D.D., et al. (2020). A RT-PCR assay for the detection of coronaviruses from four genera. J. Clin. Virol. *128*, 104391.

Zivanov, J., Nakane, T., Forsberg, B.O., Kimanius, D., Hagen, W.J., Lindahl, E., and Scheres, S.H. (2018). New tools for automated high-resolution cryo-EM structure determination in RELION-3. Elife *7*, e42166.

Zivanov, J., Nakane, T., and Scheres, S.H.W. (2019). A Bayesian approach to beam-induced motion correction in cryo-EM single-particle analysis. IUCrJ *6*, 5–17.

STAR★METHODS

KEY RESOURCES TABLE

REAGENT or RESOURCE	SOURCE	IDENTIFIER
Bacterial strains		
E. coli DH10B Competent Cells	Invitrogen	Cat# 44-0099
Deposited data		
CCoV-HuPn-2018-S swung out conformation CryoEM	https://www.ebi.ac.uk/pdbe/emdb/	PDB 7USA EMD-26730
CCoV-HuPn-2018-S proximal conformation CryoEM	https://www.ebi.ac.uk/pdbe/emdb/	PDB 7US6 EMD-26727
CCoV-HuPn-2018-D0 swung out conformation CryoEM	https://www.ebi.ac.uk/pdbe/emdb/	PDB 7USB EMD-26731
CCoV-HuPn-2018-D0 proximal conformation CryoEM map	https://www.ebi.ac.uk/pdbe/emdb/	PDB 7US9 EMD-26729
CCoV-HuPn-2018_RBD + canine APN ectodomain	https://www.rcsb.org	PDB 7U0L
Experimental models: Cell lines		
HEK293T cells	ATCC	Cat# CRL-11268
ExpiCHO cells	ThermoFisher Scientific	Cat# A29127
Oligonucleotides		
humanAPN_R741T_Fwd: aataccaacaactggacc gagatcc	Integrated DNA Technologies, Inc.	N/A
humanAPN_R741T_Rev: atttctgaagtgaatgaagagg	Integrated DNA Technologies, Inc.	N/A
canineAPN_T749R_Fwd: aactggcgggaccaccctc agacac	Integrated DNA Technologies, Inc.	N/A
canineAPN_T749R_Rev: ctgtgtgatcttctcaaagtgattg	Integrated DNA Technologies, Inc.	N/A
humanAPN_R741G_Fwd: aataccaacaactggggcgagatcc	Integrated DNA Technologies, Inc.	N/A
Recombinant DNA		
pcDNA3.1(+): CCoV-HuPn-2018_S_2P_avi_his	This study	N/A
pcDNA3.1(+): CCoV-HuPn-2018_S _Full-length	This study	N/A
pcDNA3.1(+): HCoV-229E S_Full-length	This study	N/A
pcDNA3.1(+): TGEV S_Full-length	This study	N/A
pcDNA3.1(+): CCoV-HuPn-2018_RBD domain	This study	N/A
pcDNA3.1(+): HCoV-229E RBD domain	This study	N/A
pcDNA3.1(+): TGEV RBD domain	This study	N/A
pcDNA3.1(+): human APN_full-length	This study	N/A
pcDNA3.1(+): human APN_full-length_R741T	This study	N/A
pcDNA3.1(+): canine APN_full-length	This study	N/A
pcDNA3.1(+): canine APN_full-length_T749R	This study	N/A
pcDNA3.1(+): feline APN_full-length	This study	N/A
pcDNA3.1(+): porcine APN_full-length	This study	N/A
pcDNA3.1(+): human APN_ectodomain_Fc	This study	N/A
pcDNA3.1(+): human APN_ectodomain_R741T_Fc	This study	N/A
pcDNA3.1(+): canine APN_ectodomain_Fc	This study	N/A
pcDNA3.1(+): canine APN_ectodomain_T749R_Fc	This study	N/A
pcDNA3.1(+): feline APN_ectodomain_Fc	This study	N/A
pcDNA3.1(+): porcine APN_ectodomain_Fc	This study	N/A
pcDNA3.1(+): human APN_full-length R741G	This study	N/A

(Continued on next page)

Continued

REAGENT or RESOURCE	SOURCE	IDENTIFIER
pcDNA3.1(+): CCoV-HuP_0_domain_I53-50A	This study	N/A
pcDNA3.1(+): CCoV-HuP_A_domain_I53-50A	This study	N/A
pcDNA3.1(+): CCoV-HuP_B_domain_I53-50A	This study	N/A
pCMVR: HKU1_S_I53-50A	This study	N/A
pCMVR: HA-ferritin	(Kanekiyo et al., 2013)	N/A
pCMVR: NC99-NA	(Kanekiyo et al., 2013)	N/A
TMPRSS2 plasmid	Addgene	https://www.addgene.org/53887/
Biological samples		
BirA biotin-protein ligase standard reaction kit	Avidity	Cat# 341113
Octet Kinetics Buffer (10X)	Sartorius	Cat# 18-1105
Anti-Human IgG Fc Capture (Biosensors)	Forté Bio	Cat# 18-0015
Protein A (ProA) Biosensors	Forté Bio	Cat# 18-0004
Alexa Fluor 680 goat anti-human IgG	Jackson ImmunoResearch	Cat# 109-625-098
Bio-Glo™ Luciferase Assay System	Promega	Cat# G7940
ExpiFectamine™ CHO Transfection Kit	Life technologies	Cat# A29130
Kapa HiFi HotStart Ready Mix	Roche	Cat# 7958935001
EndoFree Plasmid Mega kit	Qiagen	Cat#12381
QIAprep Spin Miniprep Kit	Qiagen	Cat#27106X4
Monarch PCR & DNA cleanup kit	New England Biolabs	Cat# T1030S
T4 DNA Ligase	New England Biolabs	Cat# M0202
T4 Ligase buffer	New England Biolabs	Cat# B0202S
Rat Red Blood Cells	Fitzgerald	88R-R002
Turkey red blood cells	Lampire	7249409
Dog red blood cells	Fitzgerald	88R-D004
Pig Red Blood Cells	Fitzgerald	88R-P002
Human red blood cells	Rockland	R407-0050
Software and algorithms		
cryoSPARC v3.0.1	(Punjani et al., 2017)	https://cryosparc.com
Relion v3.0	(Zivanov et al., 2018)	https://www3.mrc-lmb.cam.ac.uk/relion
Coot	(Emsley et al., 2010)	https://www2.mrc-lmb.cam.ac.uk/personal/pemsley/coot/
Phenix-Refine	(Liebschner et al., 2019)	https://www.phenix-online.org/download/
Phenix-Phaser	(McCoy et al., 2007)	https://www.phenix-online.org/download/
XDS	(Kabsch, 2010)	http://xds.mpimf-heidelberg.mpg.de
Prism 9	GraphPad Software	https://www.graphpad.com/scientific-software/prism/
Top Draw	(Bond, 2003)	https://bondxray.org/software/topdraw/topdraw.html
ChimeraX	(Goddard et al., 2018)	https://www.cgl.ucsf.edu/chimerax/
The ConSurf server	(Armon et al., 2001)	https://consurf.tau.ac.il/credits.php

RESOURCE AVAILABILITY

Lead contact

Further information and requests for resources and reagents should be directed to and will be fulfilled by the lead contact, David Veesler (dveesler@uw.edu).

Materials availability

Materials generated in this study will be made available on request and may require a material transfer agreement.

Data and code availability

The cryo-EM maps, X-ray diffraction data and atomic models have been deposited at the Electron Microscopy Data Bank and the Protein Data Bank with accession codes listed in the key resources tables.

EXPERIMENTAL MODEL AND SUBJECT DETAILS

Cell lines

Cell lines used in this study were obtained from ATCC: Human cells epithelial embryo (HEK293T, CRL-3216), *Felis catus* kidney cells (CRFK, CCL-94), *Canis familiaris* epithelial kidney cells (MDCK, CCL-34), *Canis familiaris* tumor fibroblast cells (A-72, CRL-1542) and *Sus scrofa* pig testis fibroblast cells (ST, CRL-1746) or ThermoFisher Scientific: ExpiCHO cells and Expi293F™ cells. Cells were cultivated at 37°C, in an atmosphere of 5 % CO_2 and with 130 rpm of agitation for suspension cells. None of the cell lines used were routinely tested for mycoplasma contamination.

Plasmids

Genes used in this study were synthesized by GenScript, codon optimized for expression in mammalian cells, cloned into pcDNA3.1 (+) between KpnI and XhoI, in frame with a Kozak's sequence to direct translation, with the signal peptide derived from the μ phosphatase: MGILPSPGMPALLSLVSLLSVLLMGCVAETGT (except for the full-length genes in which the original signal peptide was used), and avi tag and a C-terminal octa-histidine tag. CCoV-HuPn-2018-S-2P corresponds to the sequence with the entry code: QVL91811.1 and includes residues 17 to 1387. To stabilize the spike in prefusion conformation, residues E (1140) and L (1141) were mutated to P, as previously described (Pallesen et al., 2017).

Full-length wild-type S glycoproteins from HCoV-229E (AAK32191.1) residues: 1-1,155, CCoV-HuPn-2018 (QVL91811.1) residues 1-1,425 and TGEV (ABG89335.1) residues: 1-1,425, harboring C-terminal deletions of 18-, 23- and 23-residues, respectively, were used to pseudotype VSVΔG-luc. HCoV-229E, CCoV-HuPn-2018 and TGEV RBDs matching with the full-length sequences indicated above, include residues: 293 to 434, 539 to 671 and 522 to 665, respectively, fused to an avi-tag and his tag.

Full-length APNs from human (NP_001141.2), feline (NP_001009252.2), canine (NP_001139506.1) and pig (AGX93258.1) orthologs comprise residues: 1-967, 1-967, 1-975 and 1-963, respectively. APN ectodomains from human wildtype and R741T mutant (both comprising residues 66 to 967), feline (residues 64 to 967), canine (residues 71 to 975), and pig (residues 62 to 963) from the same sequence codes shown above, were fused to a thrombin cleavage site followed by a human Fc fragment tag at the C-terminal end. The 1AF10 Fab light and heavy sequences were obtained from PDB 4F2M and cloned separately into pcDNA3.1. Only the heavy chain was fused C-terminally to a sequence encoding for a GGSGGS linker and an 8 residue-long his-tag. CCoV-HuPn-2018 domain 0 (residues 17-259), domain A (residues 260-498) and domain B (residues 523-671) were fused to the N-terminus of the trimeric I53-50A nanoparticle component (Walls et al., 2020b) using a 16 residue-long glycine and serine linker.

The plasmid for expression of TMPRSS2 full-length was obtained from Addgene (https://www.addgene.org/53887/).

HKU1 S-I53-50A, NC99-NA and NC99-ferritin constructs were also synthetized by GenScript. All the protein sequences used in this study are shown in Data S1.

Mutagenesis

The wild-type full-length human APN encoding plasmid was used as a template to introduce a glycosylation sequon at position N739 (NWR to NWT) to generate human APN R741T in a PCR reaction mixture containing: 2X Kapa HiFi (Kapa biosystems) and the following primers, each at 10 μM: forward (Fwd), 5'-aataccaacaactggaccgagatcc-3' (underline is the codon change R to T) and reverse (Rev), 5'-atttctgaagtgaatgaagagg-3' from Integrated DNA Technologies (IDT). The human APN R741G mutant was generated using the same Rev primer used to generate the R741T mutant and the Fwd primer 5'-aataccaacaactggggcgagatcc-3'. Full-length wild-type canine APN encoding plasmid was used as a template to knockout the glycan at position N747 (NWT to NWR) using the primers 5'-aactggcgggaccaccctcagacac-3' (underline is the codon change T to R) and 5-ctgtgtgatcttctcaaagtgattg-3' also using the 2X Kapa HiFi (Kapa biosystems). After treating the PCR products with DpnI (New England Biolabs) during 1 h at 37°C, amplified plasmids were purified using PCR & DNA cleanup kit (Monarch) treated with T4 polynucleotide kinase (New England Biolabs) during 1 h at 37°C and ligated using T4 DNA ligase (New England Biolabs) at room temperature for 1 hour before being used for transformation to One Shot MAX Efficiency DH10B chemically competent cells (Invitrogen). Introduction of the desired mutations was verified by sequencing purified plasmids by GENEWIZ. Plasmid harboring the desired mutation were further amplified and purified with EndoFree mega kit (Qiagen) to be suitable for transfection into mammalian cells.

Protein expression and purification

To express the prefusion-stabilized CCoV-HuPn-2018 S glycoprotein, 200 ml of ExpiCHO cells grown to a density of 6×10^6/mL and 37°C, were transfected with 200 μg of CCoV-HuPn-2018-S-2P plasmid mixed with 640 l of Expifectamine CHO reagent (ThermoFisher) following manufacturer's recommendations. The day after transfection, feed and enhancer were added to the cells. Six

days post-transfection, supernatants were clarified by centrifugation at 800 g for 10 minutes. Followed addition of 20 mM imidazole, 300 mM NaCl and 20 mM Tris-HCl pH 8.0, supernatants were further centrifuged at 14,000 g for 30 min and passed through a 1 mL His trap HP column (Cytiva) previously equilibrated with binding buffer (25 mM Tris pH 7.4 and 350 mM NaCl). CCoV-HuPn-2018-S-2P was eluted using a linear gradient of 500 mM imidazole.

To express B domains from CCoV-HuPn-2018, TGEV and HCoV-229E fused to an avi- and a histidine tag, 100 ml of Expi293F cells at 3×10^6/mL were transiently transfected with 320 μl of Expifectamine and 100 μg of the respective plasmids, following the manufacturer's indications. Four days post-transfection, supernatants were clarified by centrifugation at 800 g for 10 minutes, supplemented with 20 mM imidazole, 300 mM NaCl and 25 mM Tris-HCl pH 8.0, further centrifuged at 14,000 g for 30 min and passed through a 1 mL His trap HP column (Cytiva) previously equilibrated with binding buffer (25mM Tris pH 7.4 and 350mM NaCl). B domains were eluted using a linear gradient of 500 mM imidazole. A similar protocol was used to express and purify the Fab 1AF10 fused to 8 residues histidine tag except that 50 ml of Expi293F cells were transfected with a mixture containing: 50 μg of each individual plasmid encoding the Fab light and heavy chain and 160 μl of Expifectamine.

To express APN ectodomains from human, feline, canine and pig orthologs fused to Fc portion of human IgG, Expi293F cells were transiently transfected with the respective plasmids following the manufacturer's protocols. Briefly, 50 ml of Expi293F cells at 3×10^6/mL were transfected using 160 μl of Expifectamine and 50 μg of APN plasmid. Four days after transfection, supernatants were clarified by centrifugation at 800 g for 10 minutes, supplemented with 300 mM NaCl and 25 mM Tris-HCl pH 8.0, further centrifuged at 14,000 g for 30 min and passed through a 1 mL HiTrap Protein A HP column (Cytiva). Proteins were eluted using 0.1 M citric acid pH 3.0 in individual tubes containing 200 μl of 1 M Tris-HCl pH 9.0 to immediately neutralize the low pH needed for elution. Fractions containing the proteins were pooled and buffer exchanged to 25 mM Tris-HCl pH 8.0, 150 mM NaCl. To produce APNs without the Fc fusion, the Fc fragment of all APN orthologs was removed using thrombin (Millipore Sigma) in a reaction mixture containing: 3 μg of thrombin/mg of APN-Fc, 20 mM Tris-HCl pH 8.0, 150 mM NaCl and 2.5 mM $CaCl_2$ incubated overnight at room temperature. The reaction mixture was then loaded to a Protein A column to remove uncleaved APN-Fc and the Fc tag. Monomeric APNs were further purified by size-exclusion chromatography (SEC) on a Superdex 200 column 10/300 GL (GE Life Sciences) previously equilibrated in 25 mM Tris pH 8.0 and 150 mM NaCl.

HKU1 S-I53-50A protein was produced in Expi293F cells grown in suspension using Expi293F expression medium (Life Technologies) at 33°C, 70% humidity, 8% CO2 rotating at 150 rpm. The cultures were transfected using PEI-MAX (Polyscience) with cells grown to a density of 3.0 million cells per mL and cultivated for 3 days. Supernatants were clarified by centrifugation (5 min at 4000 rpm), addition of pDADMAC solution to a final concentration of 0.0375% (Sigma Aldrich, #409014), and a second spin (5 min at 4000 rpm). HKU1-S-I53-50A protein containing His tag was purified from clarified supernatants via a batch bind method where each clarified supernatant was supplemented with 1 M Tris-HCl pH 8.0 to a final concentration of 50 mM and 5 M NaCl to a final concentration of 300 mM. Talon cobalt affinity resin (Takara) was added to the treated supernatants and allowed to incubate for 15 min with gentle shaking. Resin was collected using vacuum filtration with a 0.2 mm filter and transferred to a gravity column. The resin was washed with 20 mM Tris pH 8.0, 300 mM NaCl, and the protein was eluted with 3 column volumes of 20 mM Tris pH 8.0, 300 mM NaCl, 300 mM imidazole. The batch bind process was then repeated and the first and second elutions combined. SDS-PAGE was used to assess purity. HKU1-S-I53-50A fusion protein IMAC elution was concentrated to > 1 mg/mL and subjected to three rounds of dialysis into 50 mM Tris pH 8, 150 mM NaCl, 0.25% w/v Histidine, and 5% glycerol in a hydrated 10K molecular weight cutoff dialysis cassette (Thermo Scientific).

To produce HA-ferritin nanoparticles, 1 mg/L of NC99-ferritin vector was transiently transfected together with 0.05 mg/L of NC99 neuraminidase (NA) vector into Expi293F using polyethylenimine transfection reagent. Four days after transfection, culture supernatants were collected and sterile filtered. HA-ferritin NPs were purified by lectin affinity chromatography (EY labs), followed by size-exclusion chromatography with a Superose 6 Increase 10/300 GL (GE) in 25 mM Tris, pH 8.0, 150 mM NaCl, 5% glycerol.

Protein biotinylation

B domains from HCoV-229E, TGEV and CCoV-HuPn-2018 were biotinylated using BirA biotin-protein ligase standard reaction kit (Avidity) following manufacturer's protocol. In a typical reaction, 40 μM of B domains were incubated overnight at 4°C with 2.5 μg of BirA enzyme in reaction mixtures containing 1X BiomixB, 1X BiomixA and 40 μM BIO200. Domains B were further separated from Bir A by SEC using Superdex 75 increase 10/300 GL (GE LifeSciences) and concentrated using 10 kDa filters (Amicon).

Biolayer interferometry

APNs binding measurements to B domains were performed using Biolayer interferometry. Biotinylated B domains from CCoV-HuPn-2018, TGEV and HCoV-229E were immobilized at 1 μg/mL in undiluted 10X kinetics buffer (Pall) to streptavidin (SA) biosensors that were pre-hydrated in water for at least 10 minutes and then equilibrated into 10X Kinetics Buffer (Pall). The loaded tips were then dipped into a dilution series of APN orthologs from human (wild-type or glycan knockin R741T), feline, canine (wild-type or T749R, and porcine or 1AF10 Fab in 10X Kinetics Buffer (Pall) starting at various concentrations for 300 seconds prior to 300 seconds dissociation in 10X Kinetics buffer for kinetics determination. The data were baseline subtracted and the plots fitted using the Pall FortéBio/Sartorius analysis software (v.12.0). Data were plotted in Graphpad Prism (v.9.0.2). These experiments were done side-by-side with two different batches of B domains and APN orthologs preparations. For competition BLI experiments, CCoV-HuPn-2018 or TGEV biotinylated RBD were immobilized at 1 μg/mL in undiluted 10X kinetics buffer (Pall) to SA sensors that were

pre-hydrated in water for at least 10 minutes and then equilibrated into 10X Kinetics Buffer (Pall). B domain-loaded SA biosensors were sequentially dipped in a solution containing the 1AF10 Fab at concentrations ten times above the respective affinity (170 nM for CoV-HuPn-2018 or 100 nM for TGEV) and then in a solution containing the same concentration of 1AF10 supplemented with orthologs APN at concentrations 10X above their respective apparent affinity.

For nanoparticles experiments, canine and human R741T APN-Fc ectodomains were immobilized at the surface of protein A biosensors at 2 μg/ml and were dipped in 1 μM of CCoV-HuPn-2018-Domain0-NPs or CCoV-HuPn-2018-DomainB-NPs diluted in 10X Kinetics Buffer (Pall). Data were baseline subtracted and fit using the Pall FortéBio/Sartorius analysis software (v.12.0). Data were plotted in Graphpad Prism (v.9.0.2).

Pull-down assays

The interaction between APN orthologs and B domains was further analyzed performing a pull-down assay. Briefly, 200 μl (2 mg) of magnetic beads Dynabeads™ Strep Isolation (ThermoFisher) were washed twice with 300 μL 1X TBS-T (2.4 g Tris-Base/L, 8 g NaCl/L, 0.1 % Tween20) using a magnetic stand (ThermoFisher) before coupling them with 200 μl of B domains in TBS at 0.125 ng/ml. The mixture beads/protein were well mixed and incubated for 1h at room temperature with constant gentle rotation. Beads were then washed two times with 200 μL TBS-T before resuspending them in a solution containing an excess of 10-20X of their calculated $K_{D,app}$ using BLI, of the APN-Fc orthologs and allow binding for 1 hr at RT with gentle rotation after which were washed two times with TBS-T. Flow through, last wash and beads were collected and analyzed in SDS-PAGE gel. Control assays consisted of beads alone, i.e: not coupled to B domains.

Bacterial protein expression and purification of nanoparticles components

The I53-50A and I53-50B proteins were expressed as described before (Walls et al., 2020b). Briefly, transformed Lemo21(DE3) (NEB) in LB (10 g Tryptone, 5 g Yeast Extract, 10 g NaCl) were grown at 37°C to an OD600 ~0.8 with agitation. Expression was induced with 1 mM IPTG and temperature was reduced to 18°C. Cells were harvested after ~16 h and lysed by microfluidization using a Microfluidics M110P at 18,000 psi in 50 mM Tris, 500 mM NaCl, 30 mM imidazole, 1 mM PMSF, 0.75% CHAPS. Lysates were clarified by centrifugation at 24,000 g for 30 min and applied to a 2.6 × 10 cm Ni Sepharose 6 FF column (Cytiva) for purification by IMAC on an AKTA Avant150 FPLC system (Cytiva). Proteins were eluted with a linear gradient of 30 mM to 500 mM imidazole in 50 mM Tris pH 8, 500 mM NaCl, 0.75% CHAPS buffer. Peak fractions were pooled, concentrated in 10K MWCO centrifugal filters (Millipore), sterile filtered (0.22 μm) and applied to either a Superdex 200 Increase 10/300, or HiLoad S200 pg GL SEC column (Cytiva) previously equilibrated in 50 mM Tris pH 8, 500 mM NaCl, 0.75% CHAPS buffer.

In vitro nanoparticle assembly

Concentration of purified individual nanoparticle components was determined by measuring absorbance at 280 nm and the corresponding calculated extinction coefficients. Nanoparticles were prepared by incubation of domain A-I53-50A or domain B-I53-50A or HKU1-S-I53-50A trimers with pentameric I53-50B at molar ratios 1.1:1, respectively, in 50 mM Tris pH 8, 500 mM NaCl, 0.75% w/v CHAPS. Formation of Domain 0-NPs required mixing domain 0-I53-50A with I53-50A at a molar ratio of 1:6 with pentameric I53-50B. All *in vitro* assemblies were incubated at room temperature with gentle rocking for at least 30 min before subsequent purification by SEC on a Superose 6 column to remove residual unassembled components. Fractions were analyzed by negative stain electron microscopy and by PAGE-SDS. Assembled particles eluted in the void volume of a Superose 6 column and were pooled and stored at 4°C.

Negative stain electron microscopy

Nanoparticles diluted to 0.01 mg/mL in 50 mM Tris pH 8, 150 mM NaCl, were adsorbed to glow-discharged home-made carbon-coated copper grids for 30 seconds. The excess liquid was blotted away with filter paper (Whatman 1) and 3 μL of 2% w/v uranyl formate stain were applied to the grids. Finally, the stain was blotted away, and the grids were allowed to air dry for 1 min. Grids were imaged on a 120kV FEI Tecnai G2 Spirit with a Gatan Ultrascan 4000 4k x 4k CCD camera at 67,000 nominal magnification using a defocus ranging between 1.0 and 2.0 μm and a pixel size of 1.6 Å.

Hemagglutination assays

The hemagglutination assays was performed according to standard procedures. Briefly, 50 μl of CCoV-HuPn-2018 domain 0, domain A, domain B NPs at 400 ng/μl were incubated with 50 μl 0.5% (diluted in PBS) turkey (Lampire biological laboratories), dog (Fitzgerald), human (Rockland Immunochemicals), pig (Fitzgerald) and rat (Fitzgerald) erythrocytes in V-bottom, 96-well plates (Greiner Bio-One) for 30 min at room temperature after which plates were photographed and hemagglutination was analyzed. In another experiment, eight 2-fold dilutions starting at 200 ng/μl of CCoV-HuPn-2018 Domain 0-NPs were incubated with 50 μl 0.5% turkey, dog, human and pig erythrocytes for 30 min at room temperature after which plates were analyzed. To determine whether sialic acids were involved in the interaction, human erythrocytes were pretreated for 3 h at 37 °C with neuraminidase (NA) from A. ureafaciens (Roche; diluted to 30 mU/mL in PBS), before incubation with different concentrations of CCoV-HuPn-2018 Domain 0-NPs for 1 h at room temperature. HKU1-S-NP at 220 ng/μl and HA-ferritin at 400 ng/μl were used as positive controls when incubated with 0.5% rat and turkey erythrocytes, respectively.

VSV pseudotyped virus production

CCoV-HuPn, HCoV-229E (AAK32191.1, P100E isolate) and TGEV S pseudotyped VSV were generated as previously described (Tortorici et al., 2020, 2021). Briefly, HEK293T cells in DMEM supplemented with 10% FBS and 1% PenStrep and seeded in poly-D-lysine coated 10-cm dishes were transfected with a mixture of 24 μg of the corresponding plasmid encoding for: CCoV-HuPN S, TGEV S or HCoV-229 S, 60 μl Lipofectamine 2000 (Life Technologies) in 3 ml of Opti-MEM, following manufacturer's instructions. After 5 h at 37°C, DMEM supplemented with 20% FBS and 1% PenStrep was added. The next day, cells were washed three times with DMEM and were transduced with VSVΔG-luc (Kaname et al., 2010). After 2 h, virus inoculum was removed and cells were washed five times with DMEM prior to the addition of DMEM supplemented with anti-VSV-G antibody [Il-mouse hybridoma supernatant diluted 1 to 25 (v/v), from CRL-2700, ATCC] to minimize parental background. After 18-24 h, supernatants containing pseudotyped VSV were harvested, centrifuged at 2,000 x g for 5 minutes to remove cellular debris, filtered with a 0,45 μm membrane, concentrated 10 times using a 30 kDa cut off membrane (Amicon), aliquoted, and frozen at -80°C.

Pseudotyped VSV infections and neutralizations

For pseudotyped VSV infections and neutralizations, HEK293T cells were transfected with plasmids encoding for the different full-length APN orthologs (flAPN) following the protocol described by Eguia et al. (2021). Briefly, HEK293T cells at 90% confluency and seeded in poly-D-lysine coated 10-cm dishes were transfected with a mixture in Opti-MEM containing 8 μg of the corresponding plasmid encoding flAPN ortholog, 1 μg of the plasmid encoding full-length TMPRSS2 and 30 μl of Lipofectamine 2000 (Life Technologies) according to the manufacturer's instructions. After 5 h at 37°C, cells were trypsinized, seeded into poly-D-lysine coated clear bottom white walled 96-well plates at 40,000-50,000 cells/well and cultured overnight at 37°C. For infections, 5-10 μl of the corresponding pseudotyped VSV were mixed with 35-30 μl of DMEM and the mixture was added to the cells previously washed three times with DMEM. After 2 h at 37°C, 40 μl of DMEM were added and cells were further incubated overnight at 37°C. For neutralizations, eleven 2-fold serial dilutions of Fab 1AF10, APN ectodomains orthologs or sera, were prepared in DMEM. 20 μl of CCoV-HuPn-2018 S, HCoV-229E S or TGEV S pseudotyped VSV were added 1:1 (v/v) to each Fab1AF10, APN ectodomains or sera dilution and mixtures were incubated for 45-60 min at 37°C. After removing their media, transfected HEK293T cells were washed three times with DMEM and 40 μL of the mixture containing virus:Fab/APN ectodomains/sera were added. One hour later, 40 μL DMEM were added to the cells. After 17-20 h, 60 μL of One-Glo-EX substrate (Promega) were added to each well and incubated on a plate shaker in the dark. After 5-15 min incubation, plates were read on a Biotek plate reader. Measurements were done in duplicate with at least two biological replicates and one representative experiment is shown. Relative luciferase units were plotted and normalized in Prism (GraphPad): cells alone without pseudotyped virus was defined as 0 % infection, and cells with virus only (no sera) was defined as 100 % infection.

Most of the human sera was collected from prospective bone marrow donors in Seattle with approval from the Human Subjects Institutional Review Board in the 1980s and were stored in the Infectious Disease Sciences Biospecimen Repository at the Vaccine and Infectious Disease Division of the Fred Hutch Cancer Center. A few of the sera (the ones prefixed "FH") are residual samples from Bloodworks Northwest that were collected from adults in Seattle.

Western blot

15 μl of pseudotyped VSV were mixed with 4X SDS-PAGE loading buffer, run on a 4%–15% gradient Tris-Glycine Gel (BioRad) and transferred to a PVDF membrane using the protocol mix molecular weight of the Trans-Blot Turbo System (BioRad). The membrane was blocked with 5% milk in TBS-T (20 mM Tris-HCl pH 8.0, 150 mM NaCl) supplemented with 0.05% Tween-20 at room temperature and with agitation. After 1 h, the fusion-peptide-specific S2S8 monoclonal antibody was added at 1:250 dilution and incubated overnight at 4°C with agitation. Next day, the membrane was washed three times with TBS-T and an Alexa Fluor 680-conjugated goat anti-human secondary antibody (1:50,000 dilution, Jackson ImmunoResearch, 109-625-098) was added and incubated during 1 h at room temperature. Membrane was washed three times with TBS-T after which a LI-COR processor was used to develop the western blot.

Crystallization, data collection, structure determination and analysis

Crystals of the CCoV-HuPn-2018-B domain-canine APN complex were obtained at 20°C by sitting drop vapor diffusion. 15 mg/ml canine APN were incubated with 3 mg/ml CCoV-HuPn-2018-B domain for 1 hour at room temperature before mixing with mother liquor solution (200 nl final volume) containing 0.1 M Na_2HPO_4-citric acid pH 4.2, 1.6 M Na_2HPO_4/K_2HPO_4. Crystals were flash frozen in liquid nitrogen using 30% glycerol as cryoprotectant. Diffraction data were collected at the Advanced Light Source synchrotron beamline 5.0.2 and processed with the XDS software package (Kabsch, 2010). Initial phases were obtained by molecular replacement using Phenix-Phaser (McCoy et al., 2007) and the following models: porcine APN (PDB 4f5c) and CCoV-HuPn-2018-B domain obtained by cryo-EM in this study. Several subsequent rounds of model building, and refinement were performed using Coot (Emsley et al., 2010) and Phenix-Refine (Liebschner et al., 2019) to arrive at a final model for the binary complex at 3.3 Å resolution in space group P21221. Model validation was done using Molprobity (Chen et al., 2010) and Privateer (Agirre et al., 2015).

CryoEM sample preparation, data collection and data processing

3 μl of CCoV-HuPn-2018 S at approximately 0.3 mg/ml were loaded three times onto freshly glow-discharged lacey grids covered with a thin layer of home-made continuous carbon prior to plunge freezing using a vitrobot MarkIV (ThermoFisher Scientific) with a blot force of -1 and 2.5 sec blot time at 100% humidity and 21°C.

Data were acquired using the Leginon software (Suloway et al., 2005) to control a FEI Titan Krios transmission electron microscope operated at 300 kV equipped with a Gatan K3 direct detector and a Gatan Quantum GIF energy filter, operated with a slit width of 20eV. The dose rate was adjusted to 3.75 counts/super- resolution pixel/s, and each movie was acquired in 75 frames of 40 ms with a pixel size of 0.843 Å and a defocus range comprised between 0.8 and 2.0 μm. Movie frame alignment, estimation of the microscope contrast-transfer function parameters, particle picking and extraction were carried out using Warp (Tegunov and Cramer, 2019). Two rounds of reference-free 2D classification were performed using cryoSPARC (Punjani et al., 2017) with binned particles to select well-defined particle images. Subsequently, one round of 3D classification with 50 iterations, using an ab initio-generated reference model (angular sampling 7.5° for 25 iterations and 1.8° with local search for 25 iterations) was carried out using Relion (Zivanov et al., 2018) without imposing symmetry. 3D refinements were carried out using non-uniform refinement in cryoSPARC (Punjani et al., 2020). Particle images were subjected to Bayesian polishing (Zivanov et al., 2019) using Relion during which particles were re-extracted with a box size of 512 pixels at a pixel size of 0.843 Å which was followed by another round of non-uniform refinement in cryoSPARC followed by per-particle defocus refinement and again non-uniform refinement. To improve the density of the domain 0, particles were symmetry-expanded and subjected to a Relion focus 3D classification without refining angles and shifts using a soft mask encompassing domain 0. Local refinement, local resolution estimation, filtering, and sharpening were carried out using CryoSPARC. Reported resolutions are based on the gold-standard Fourier shell correlation using 0.143 criterion (Rosenthal and Henderson, 2003) and Fourier shell correlation curves were corrected for the effects of soft masking by high-resolution noise substitution (Chen et al., 2013).

CryoEM model building and analysis

UCSF Chimera (Pettersen et al., 2004) and Coot (Emsley et al., 2010) were used to fit atomic models (PDB 5SZS) into the cryoEM maps and Domain 0 was manually built. Models were refined and rebuilt into the maps using Coot and Rosetta (Frenz et al., 2019; Wang et al., 2016). Model validation was done using Molprobity (Chen et al., 2010) and Privateer (Agirre et al., 2015). Figures were generated using UCSF ChimeraX (Goddard et al., 2018). Topology diagrams were generated using the program TopDraw (Bond, 2003).

Assessment of human *ANPEP* diversity

We assessed human diversity at or near the APN NWT motif (NWR in human; R741) in gnomAD (https://gnomad.broadinstitute.org/gene/ENSG00000166825). Observations in approximately 125,000 humans included one heterozygous N738K, one heterozygous R741G and one heterozygous I743N. No rare defects in *ANPEP* are described in OMIM (https://www.omim.org/entry/151530)
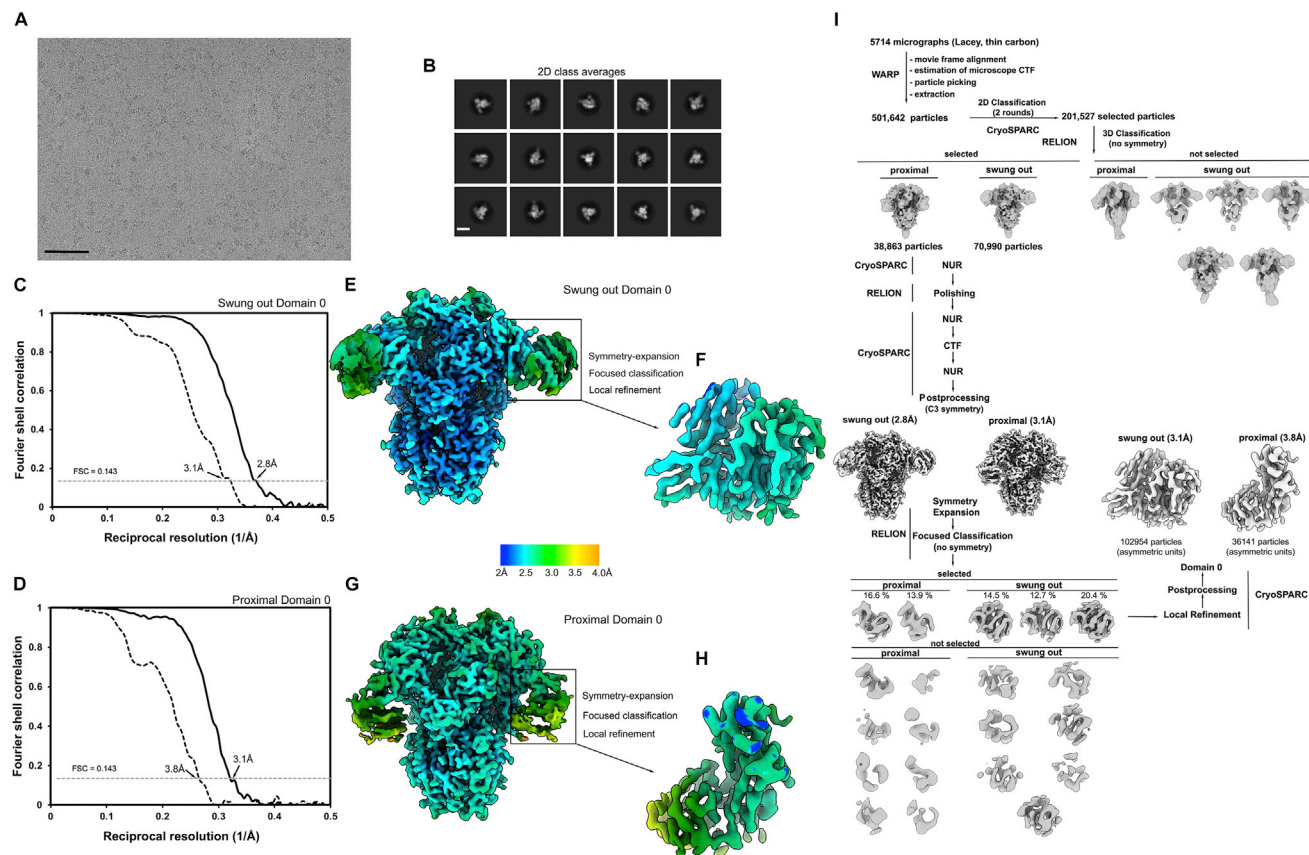
Supplemental figures

Figure S1. Data processing and validation of the CCoV-HuPn-2018 S cryo-EM dataset, related to Figures 1 and 2

(A and B) Representative electron micrograph (A) and class averages (B) of CCoV-HuPn-2018 S embedded in vitreous ice. Scale bar of the micrograph, 500 Å. Scale bar of the class averages, 100 Å.

(C and D) Gold-standard Fourier shell correlation curves for the CCoV-HuPn-2018 S trimer (solid black line) and the locally refined reconstruction of the CCoV-HuPn-2018 S domain 0 (dashed black line) for the swung out conformation (C) and the proximal conformation (D). The 0.143 cutoff is indicated by a horizontal dashed gray line.

(E–H) Local resolution maps for the CCoV-HuPn-2018 S trimer and the locally refined reconstruction of the domain 0 in the swung-out conformation (E and F) and in the proximal conformation (G and H).
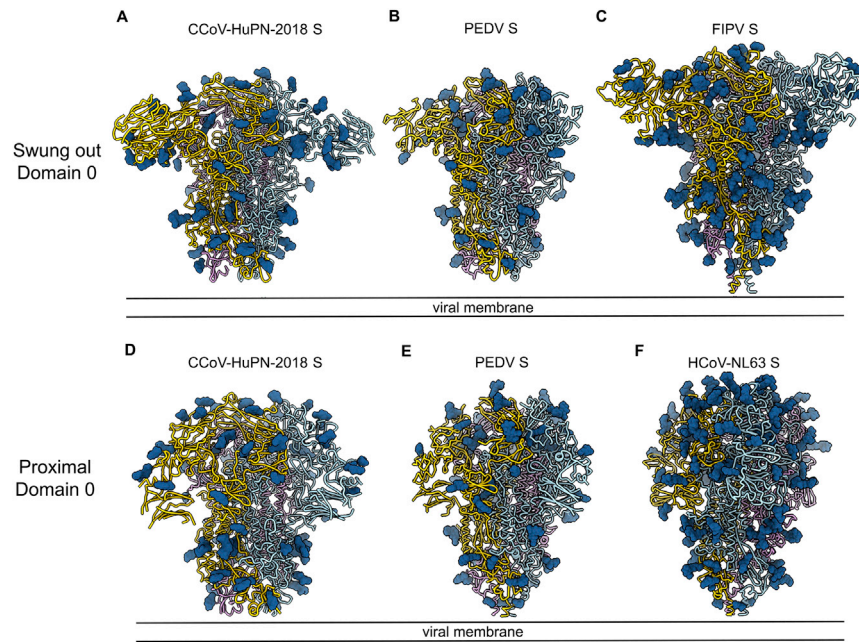
(I) Cryo-EM data processing flowchart.

Figure S2. Architecture of α-coronavirus S trimers harboring a domain 0, related to Figures 1 and 2

(A–F) Side views of CCoV-HuPn-2018 S with the two conformations of domain 0 (A and D), PEDV S (B, PDB 6VV5), FIPV S (C, PDB 6JX7), PEDV S (E, PDB 6U7K), HCoV-NL63 S (F, PDB 5SZS) perpendicular to the molecular 3-fold axis. Each α-coronavirus S protomer is colored distinctly (light blue, pink, and gold). N-linked glycans are shown as blue spheres. Renderings in (A) and (D) use composite models obtained from the global and local refinements for each conformation.
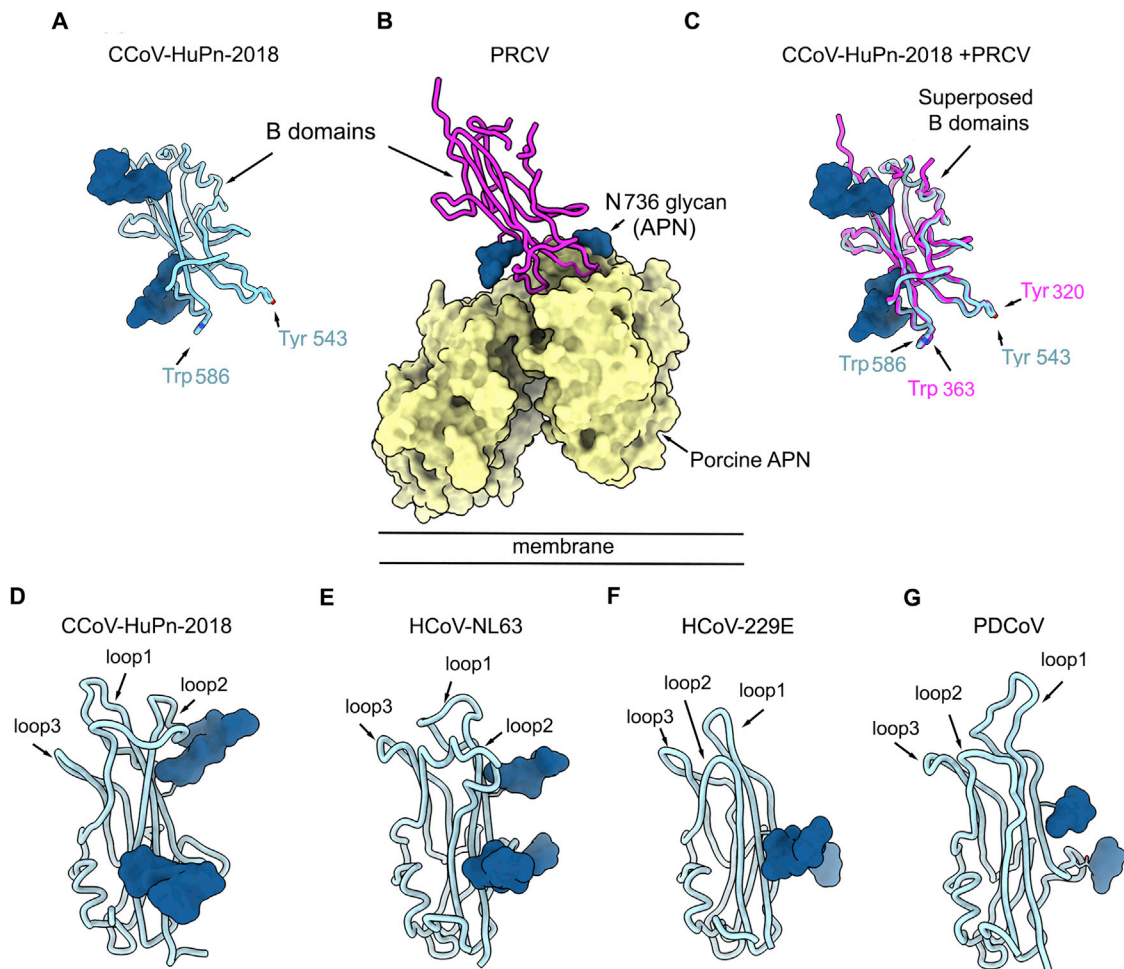
Figure S3. Architecture of α-coronavirus B domains, related to Figures 1 and 4

(A–C) Ribbon diagrams of the CCoV-HuPn-2018 B domain crystal structure (A), the PRCV B domain bound to porcine APN (PDB: 4F5C) (B), and overlay (C) underscoring their structural similarity. N-linked glycans are rendered as blue spheres.

(D–G) Ribbon diagrams of B domains from CCoV-HuPn-2018 (D), HCoV-NL63 (PDB 5SZS) (Walls et al., 2016b) (E), HCoV-229E (PDB 6ATK) (Wong et al., 2017) (F), and PDCoV (PDB 6BFU) (Xiong et al., 2018) (G). All B domains are colored light blue and N-linked glycans are rendered as blue spheres. The receptor-binding loops are indicated.

A Domain 0-NP

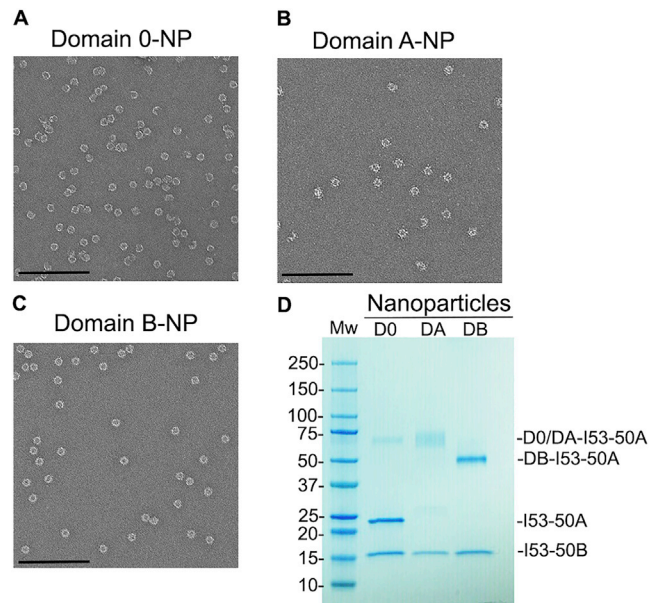**B** Domain A-NP

C Domain B-NP

D Nanoparticles

Figure S4. Characterization of CCoV-HuPn-2018 domain 0-, A-, and B-I53-50 nanoparticles, related to Figure 3

Nanoparticles (NPs) were prepared by incubation of domain 0-I53-50A, domain A-I53-50A, or domain B-I53-50A trimers with pentameric I53-50B at molar ratios of 6 (1-μM domain 0-I53-50A + 5-μM I53-50A):1 1:1 and 1:1, respectively, for 30 min at room temperature. Formation of the domain-0-containing NPs required mixing domain 0-I53-50A and I53-50A, whereas only domain A-I53-50A or domain B-I53-50A were used (besides I53-50B) for assembly of domain-A- or domain-B-containing NPs, respectively.

(A–C) Representative electron micrographs of negatively stained CCoV-HuPn-2018 domain 0-, A-, or B-I53-50 NPs. Scale bars, 200 nm.

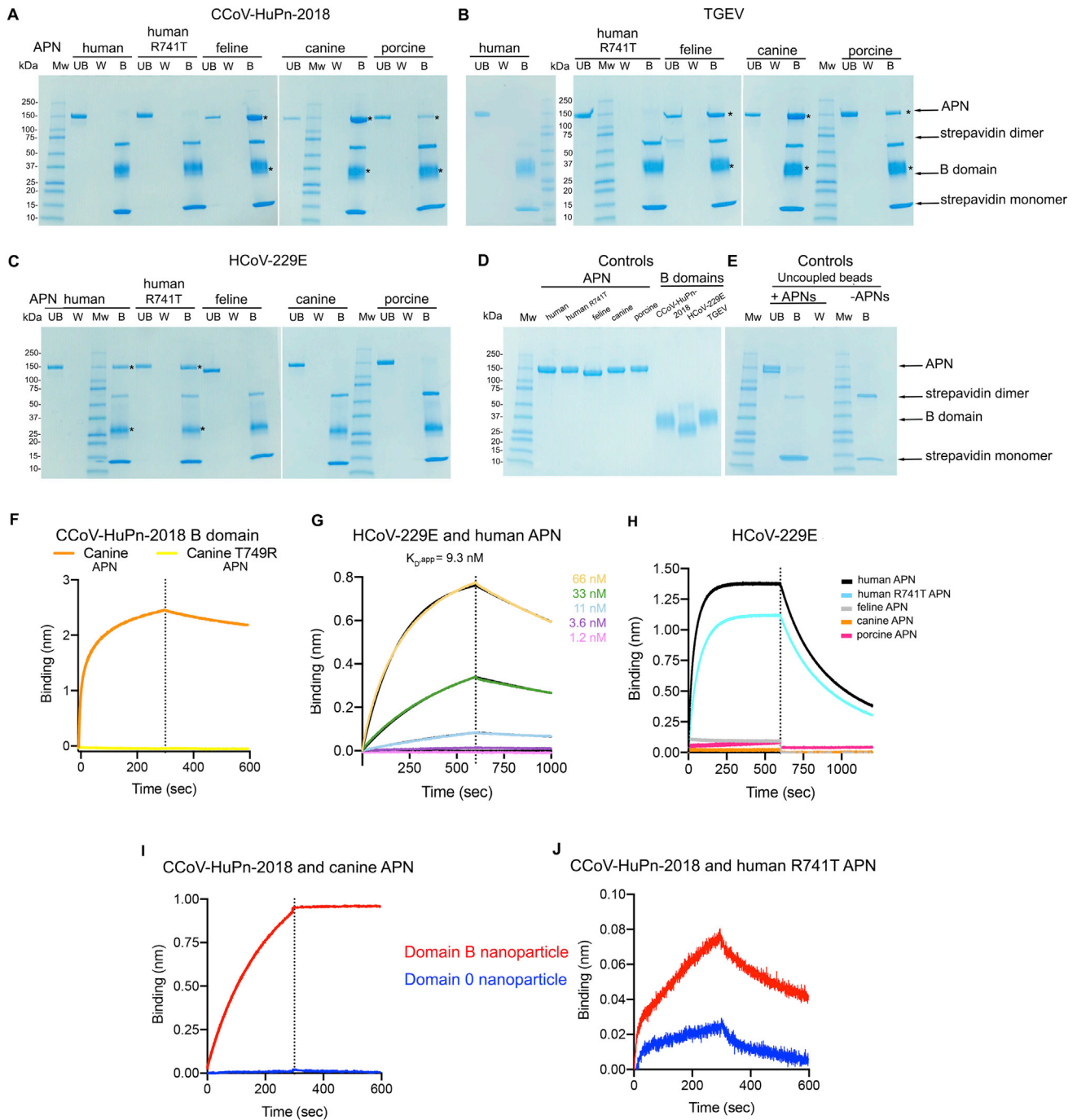(D) SDS-PAGE analysis of purified nanoparticles.

A CCoV-HuPn-2018

B TGEV

C HCoV-229E

D Controls

E Controls

F CCoV-HuPn-2018 B domain

G HCoV-229E and human APN

H HCoV-229E

I CCoV-HuPn-2018 and canine APN

J CCoV-HuPn-2018 and human R741T APN

Figure S5. The CCoV-HuPn-2018 B domain recognizes APN, related to Figures 4 and 5

(A–E) Coomassie-stained SDS-PAGE analysis of pull-downs between biotinylated B domains from CCoV-HuPn-2018 (A), TGEV (B), and HCoV-229E (C) immobilized on magnetic streptavidin beads and APN-Fc orthologs. Asterisks indicate the positions of the pulled down APN/B domain complex. UB, unbound; W, wash; B, bound. Purified proteins used in the pull-down assay (D) and beads without B domain (uncoupled) incubated or not with APNs analyzed by Coomassie-stained SDS-PAGE (E) are also shown.

(F) Biolayer interferometry binding analysis of 1-μM wildtype or T749R canineAPN-Fc (glycan knockout) to biotinylated CCoV-HuPn-2018 B domain immobilized at the surface of SA biosensors.

(G) Biolayer interferometry kinetic binding analysis of human APN-Fc to biotinylated HCoV-229E B domain immobilized at the surface of SA biosensors.

(H) Biolayer interferometry binding analysis of 1 μM human, human R741T, feline, canine, and porcine APN ectodomains (with cleaved Fc fragment) to biotinylated HCoV-229E B domain immobilized at the surface of SA biosensors.

(I and J) Biolayer interferometry binding analysis of CCoV-HuPn-2018 domain B- or domain 0-I53-50 nanoparticles to canine APN-Fc (I) or human R741T (J) APN-Fc ectodomains, immobilized at the surface of protein A biosensors.
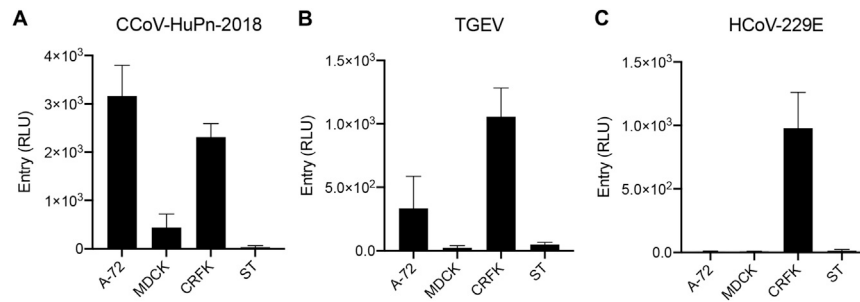
Figure S6. Cell tropism of CCoV-HuPn-2018, TGEV, and HCoV-229E S pseudoviruses, related to Figure 5

(A–C) Evaluation of pseudotyped virus mediated entry in feline, canine, and porcine cell lines. CCoV-HuPn-2018 S (A), TGEV S (B), and HCoV-229E S (C) VSV pseudotyped virus entry in *Canis familiaris* tumor fibroblast cells (A-72), *Canis familiaris* Madin-Darby canine kidney (MDCK), and *Felis catus* Crandell-Rees feline kidney (CRFK) epithelial kidney cells and *Sus scrofa* pig testis fibroblast cells (ST). Mean and standard deviation of technical duplicates are graphed.

A

CCoV-HuPn-2018

B

TGEV

C

HCoV-229E

Entry (RLU)

Plasma dilution (log$_{10}$)

D
CCoV-HuPn-2018
K$_D$=17 nM

55.6 nM
18.5 nM
6.17 nM
2.05 nM
0.68 nM

E
TGEV
K$_D$=10 nM

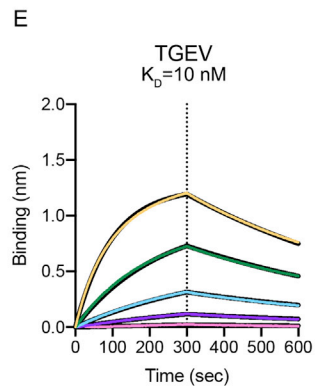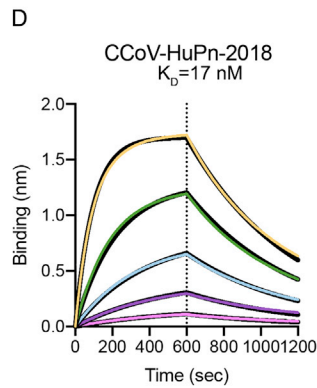Binding (nm)

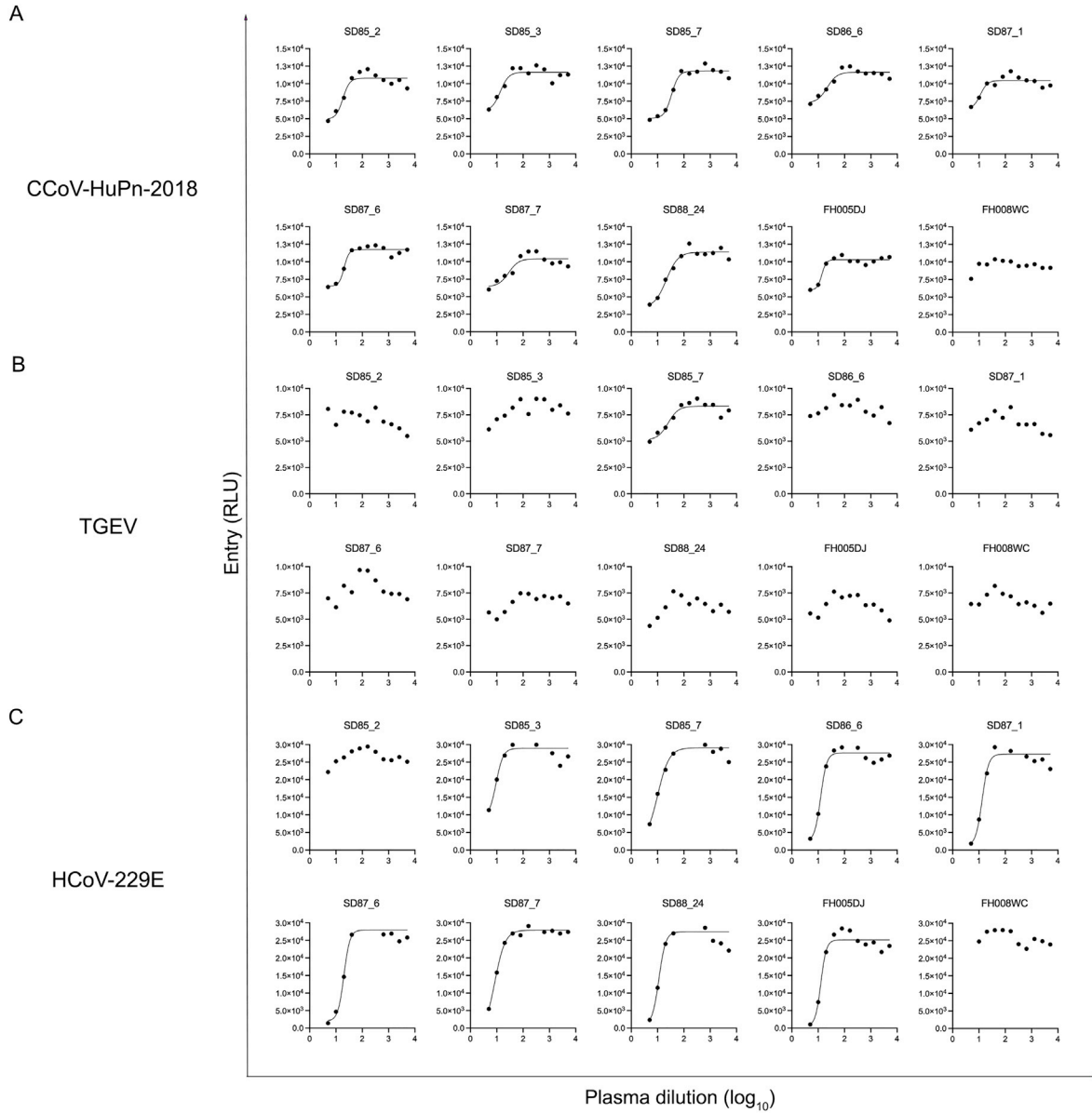Time (sec)

(legend on next page)

Figure S7. Inhibition of CCoV-HuPn-2018-S-mediated entry into cells by human polyclonal plasma antibodies and binding of CCoV-HuPn-2018 B domain to a monoclonal antibody, related to Figure 6

(A–C) CCoV-HuPn-2018 (A), TGEV (B), and HCoV-229E (C) S VSV pseudotyped mediated entry in the presence of various dilutions of plasma (name of the sample is indicated at the top of each graph) obtained between 1985 and 1989 from human subjects previously infected with HCoV-229E. One representative experiment out of two biological replicates is shown. Fits are shown only when inhibition of entry was observed.

(D and E) Biolayer interferometry kinetic analysis of 1AF10 Fab binding at various concentrations to biotinylated CCoV-HuPn-2018 (D) or TGEV (E) B domains immobilized at the surface of SA biosensors.
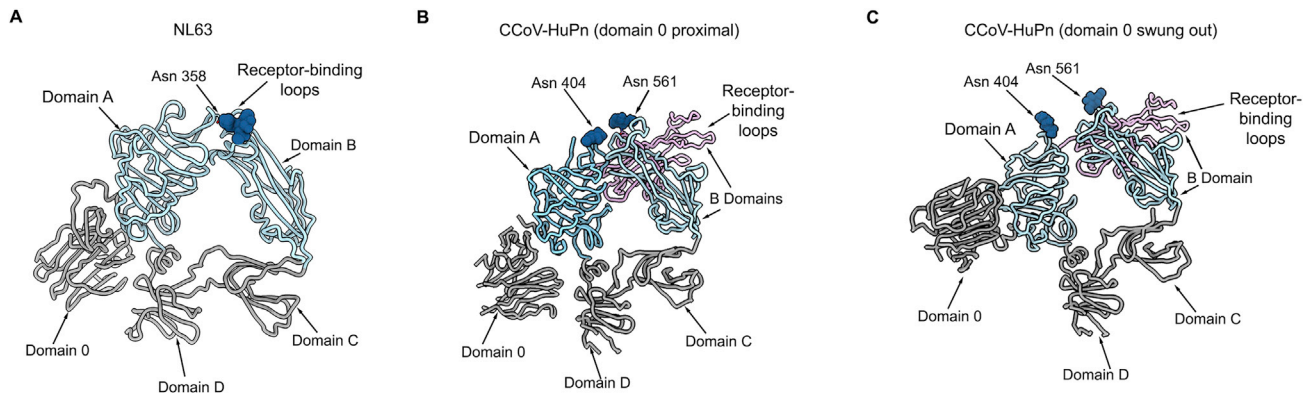
A NL63

B CCoV-HuPn (domain 0 proximal)

C CCoV-HuPn (domain 0 swung out)

Figure S8. Glycan-mediated immune evasion strategy of α-coronaviruses, related to Figure 1

(A–C) Ribbon diagrams of S_1 subunits from HCoV-NL63 S (PDB 5SZS) (A) and from CCoV-HuPn-2018 S with domain 0 in proximal (B) or swung out (C) conformations. The HCoV-NL63 receptor-binding loops are buried through interactions with domain A of the same protomer (light blue), including the glycan moiety at Asn358, and are not available to engage host cell receptors. The CCoV-HuPn-2018 receptor-binding loops are also buried by interactions with domain A, including the glycan at position N404 of the same protomer (light blue) and N561 from another protomer (pink). Renderings in (B) and (C) use composite models obtained from the global and local refinements for each conformation.